Journal of Geochemical Exploration 199 (2019) 60–74

Contents lists available at ScienceDirect

Journal of Geochemical Exploration

journal homepage: www.elsevier.com/locate/gexplo

Mechanism of gold precipitation in the Gezigou gold deposit, Xinjiang, NW China: Evidence from fluid inclusions and thermodynamic modeling

Huichao Zhang[a,b], Yongfeng Zhu[a,*]

[a] Key Laboratory of Orogenic Belts and Crustal Evolution, School of Earth and Space Sciences, Peking University, Beijing 100871, China
[b] Institute of Geology, Chinese Academy of Geological Sciences, Beijing 100037, China

ARTICLE INFO

Keywords:
Gold deposit
Arsenopyrite
Fluid inclusions
Thermodynamic modeling
West Junggar China

ABSTRACT

The Gezigou gold deposit, which is located in west Junggar (Xinjiang, China), is mainly hosted in graphite-bearing siltstone. These ore bodies, which consist of gold-bearing hydrothermal veins and mineralized siltstone with disseminated sulfides, formed in three stages: quartz-sulfides-native gold (I), arsenopyrite-calcite-native gold (II), and quartz-calcite (III) stages. The microthermometric and laser Raman spectroscopic analysis of the fluid inclusions in stage I-quartz demonstrate that the ore-forming fluid was moderate temperature (353–392 °C), low-salinity (2.9–5.3 wt% NaCl equiv.), and H_2O-CH_4-dominant. The thermodynamic modeling of the Au-Cu-As-Fe-S system performed using the SUPCRT92 software package with the updated database of slop16.dat indicates that a decrease in H_2S activity (a_{H2S}) and oxygen fugacity (fO_2) were responsible for reducing the solubilities of As and Au, which might be responsible for the coexistence of arsenopyrite and native gold. The decreases in a_{H2S} and fO_2 caused by phase separation and fluid-rock reactions induced the precipitation of native gold in the quartz-sulfides-native gold stage. Graphite-bearing siltstone, which may lower the fO_2 of ore-forming fluids, is thus an important indicator of prospective gold deposits.

1. Introduction

Sulfides are the most common gold-bearing minerals in hydrothermal gold deposits. The texture, paragenesis, and composition of sulfides may provide insight into the characteristics of ore-forming fluids and the evolution of ore-forming systems (Reich et al., 2013; Deditius et al., 2014; Wang and Zhu, 2015; Rottier et al., 2016; Zhong et al., 2018). Pyrite and arsenopyrite are ubiquitous in hydrothermal gold deposits. The close relationship between pyrite and native gold has been widely studied (Large et al., 2009; Velásquez et al., 2014; Wang et al., 2017). The texture and chemical composition of pyrite have been used to illustrate the ore-forming processes and mechanisms of gold mineralization (Fleet and Mumin, 1997; Morey et al., 2008; Pitcairn et al., 2015; Wang and Zhu, 2015; Liu et al., 2015; Qiu and Zhu, 2015; An and Zhu, 2018). The close relationship between arsenopyrite and native gold has also been reported in some hydrothermal gold deposits (Oberthür et al., 1997; Kovalev et al., 2011; Cook et al., 2013; Salvi et al., 2016), but studies of the formation conditions of coexisting arsenopyrite and native gold are rare. The Gezigou gold deposit, which is located in west Junggar, Xinjiang, comprises gold-bearing hydrothermal veins and mineralized siltstone with disseminated sulfides. Notably, these ore bodies contain abundant arsenopyrite, which is the only gold-bearing sulfide. Therefore, it is very meaningful to investigate the characteristics and ore-forming processes of this type of gold deposit, as such deposits contain abundant arsenopyrite.

Here, we provide detailed geological and mineralogical data, and the results of fluid inclusion analyses in order to illustrate the ore-forming process and mechanism of gold precipitation of the Gezigou gold deposit. Thermodynamic modeling based on the observed mineral assemblages and physicochemical conditions of the ore-forming fluid was applied to explain the co-precipitation of native gold and arsenopyrite.

2. Regional geology

West Junggar is located in the central region of the Central Asian Orogenic Belt, and it underwent multi-stage geological evolution. A number of metallic ore deposits have been discovered in this area, including the Baogutu porphyry copper-gold deposit, the Sartohay chromite deposit, and several gold deposits in the Hatu-Baobei volcanic-sedimentary basin (Fig. 1a–b; Zhu et al., 2013a). West Junggar is characterized by a series of complex ophiolite mélanges that formed during the early Paleozoic (Fig. 1b; Ren et al., 2014; Zhu et al., 2013b). The Darbut fault is a major sinistral NE-E-trending zone that separates

* Correspondence to: Y. Zhu, School of Earth and Space Sciences, Peking University.
E-mail addresses: zhanghch@126.com (H. Zhang), yfzhu@pku.edu.cn (Y. Zhu).

https://doi.org/10.1016/j.gexplo.2019.01.014
Received 18 June 2018; Received in revised form 8 December 2018; Accepted 23 January 2019
Available online 25 January 2019
0375-6742/

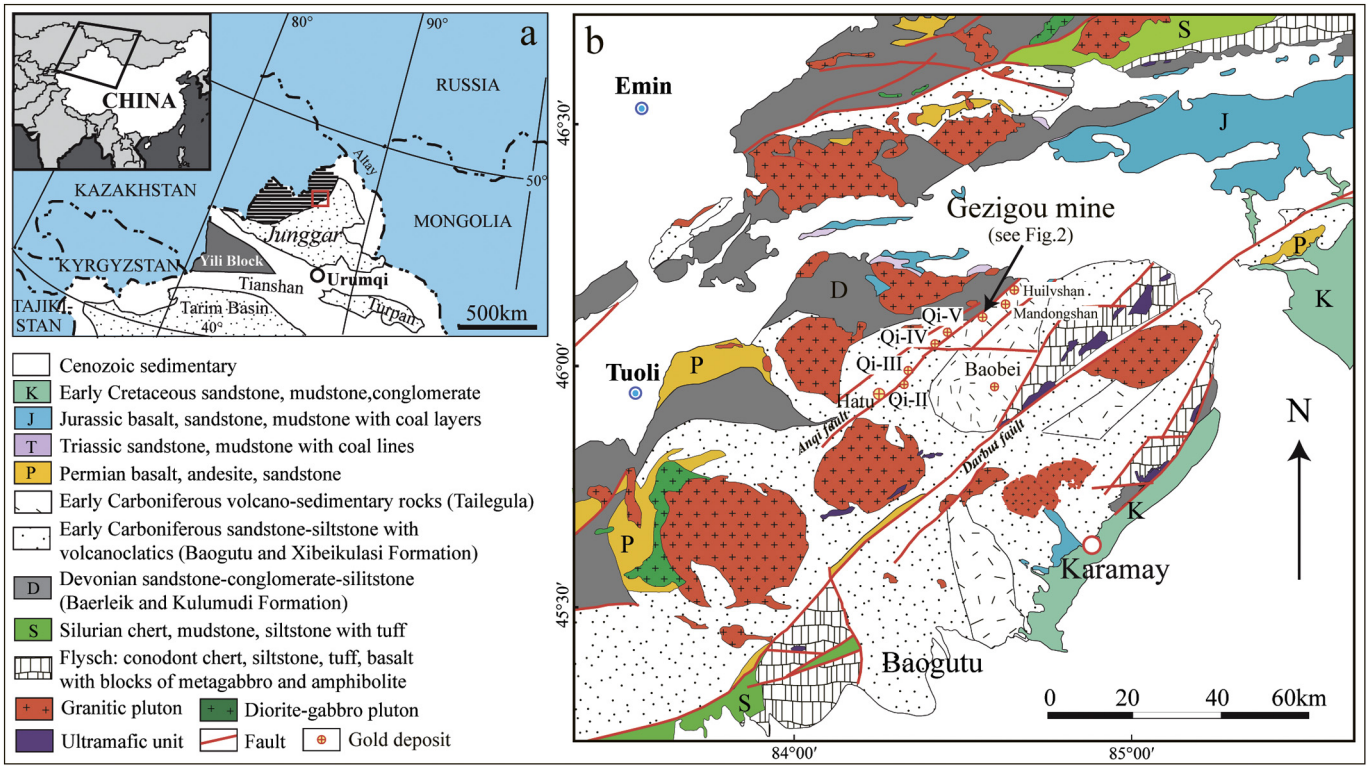

Fig. 1. (a) Schematic map showing the location of west Junggar. (b) Geological map of west Junggar, modified after Zhu et al. (2013b).

the volcanic-sedimentary rocks from the ophiolitic mélange containing a chaotic assemblage of blocks of strongly deformed serpentinite, metagabbro, chert, and basalt. Serpentinite with chromitite lenses occasionally occurs at the stratigraphic base of the Sartohay ophiolitic mélange (Zhu et al., 2016; Zhu, 2017). These ophiolitic mélanges and associated flysch containing chert and siltstone, are unconformably covered by Devonian-Early Carboniferous volcanic-sedimentary rocks (Fig. 1b). The Early Carboniferous volcanic-sedimentary rocks composed of the Xibeikulasi, Baogutu, and Tailegula Formations are widely distributed in west Junggar. The Xibeikulasi Formation is mainly composed of breccia-bearing sandstone and tuffaceous siltstone; the Baogutu Formation is primarily composed of tuffaceous siltstone and tuff with a U-Pb age of 328–342 Ma (An and Zhu, 2009); and the Tailegula Formation consists of jasper, siltstone, intermediate-basic volcanics, and tuff dated to be 328 Ma (Wang and Zhu, 2007). Late Carboniferous to Early Permian intermediate to granitic intrusions and mafic dykes intruded into the ophiolite mélanges and Devonian to Early Carboniferous volcanic-sedimentary rocks (Han et al., 2006; Zhu et al., 2013b; Zhang and Zhu, 2018).

The Hatu-Baobei volcanic-sedimentary basin, which is located between the Hatu and Darbut faults, contains several gold deposits, including the Hatu, Qi-III, Baobei, Huilvshan, Mandongshan, and Gezigou deposits (Zhu et al., 2014). Most of these gold deposits are distributed along the NNE-trending Anqi fault or its subordinate faults. The Huilvshan-Mandongshan gold district, which contains the Huilvshan, Mandongshan, and Gezigou gold deposits, is located in the northeastern region of the Hatu-Baobei volcanic-sedimentary basin (Fig. 1b). Pyrite is the predominant sulfide in most of the gold deposits in west Junggar, such as Hatu, Qi-III, and Huilvshan (An and Zhu, 2007; Wang and Zhu, 2015; Shen et al., 2016; Zhang and Zhu, 2016). However, the Gezigou gold deposit is characterized by abundant arsenopyrite, which is the only gold-bearing sulfide in this gold deposit, similar to the adjacent Mandongshan gold deposit (Zhang and Zhu, 2017).

3. Geology of the Gezigou gold deposit

The Gezigou gold deposit, which is located in the southwestern section of the Huilvshan-Mandongshan gold district, contains nearly 3.4 t of total gold resources with an average grade of 3.7 g/t (China National Gold Group Corporation Geology Co., Ltd, 2014). The main wall rocks exposed in the Gezigou mine are Lower Carboniferous siltstone and breccia-bearing sandstone. The breccia-bearing sandstone strata are in conformable contact with siltstone and commonly have siltstone interlayers. These strata are NE-trending and dip steeply to the SE at 45–75° (Fig. 2a). The main host rock is siltstone, which mainly consists of quartz and calcite with minor sericite, chlorite, and graphite. The grain size of quartz commonly ranges from 0.03 to 0.05 mm. The breccia-bearing sandstone is composed of quartz and plagioclase with minor chlorite and epidote, and the breccia is mainly siltstone breccia with the sizes ranging from 2 to 5 mm. Most of plagioclase grains have experienced sericitization. Although a small amount of the breccia-bearing sandstones have experienced hydrothermal alteration and host quartz-sulfides veins, the veins in the breccia-bearing sandstone are relatively thin (< 5 mm) and have limited economic significance. Most of the siltstone contains some subparallel graphite-bearing belts, which represent favorable locations for high-grade ores. From north to south, the Gezigou gold deposit comprises three ore bodies: L1, L3, and L5 (Fig. 2a). These ore bodies mainly consist of gold-bearing hydrothermal veins and sulfides-bearing mineralized siltstone. The main sulfides in these ore bodies include arsenopyrite, pyrite, chalcopyrite, and sphalerite. The L1 ore body, which is located in the northern part of the mine, is approximately 40 m long, 0.8–2.0 m thick, and extends over 40 m in depth, striking NE and dipping to the SE at 88–90°. The L3 ore body, which is located to the south of the L1 ore body, is approximately 500 m long, 1.2–6.0 m thick, and extends over 140 m in depth, striking nearly NNE and dipping to the SE at 65–85°. The L5 ore body, which is located to the southeast of the L3 ore body, is approximately 500 m long, 2.0–3.1 m thick, and extends 50 m in depth, striking nearly NEE and dipping to the SE at 50–70° (China National Gold Group

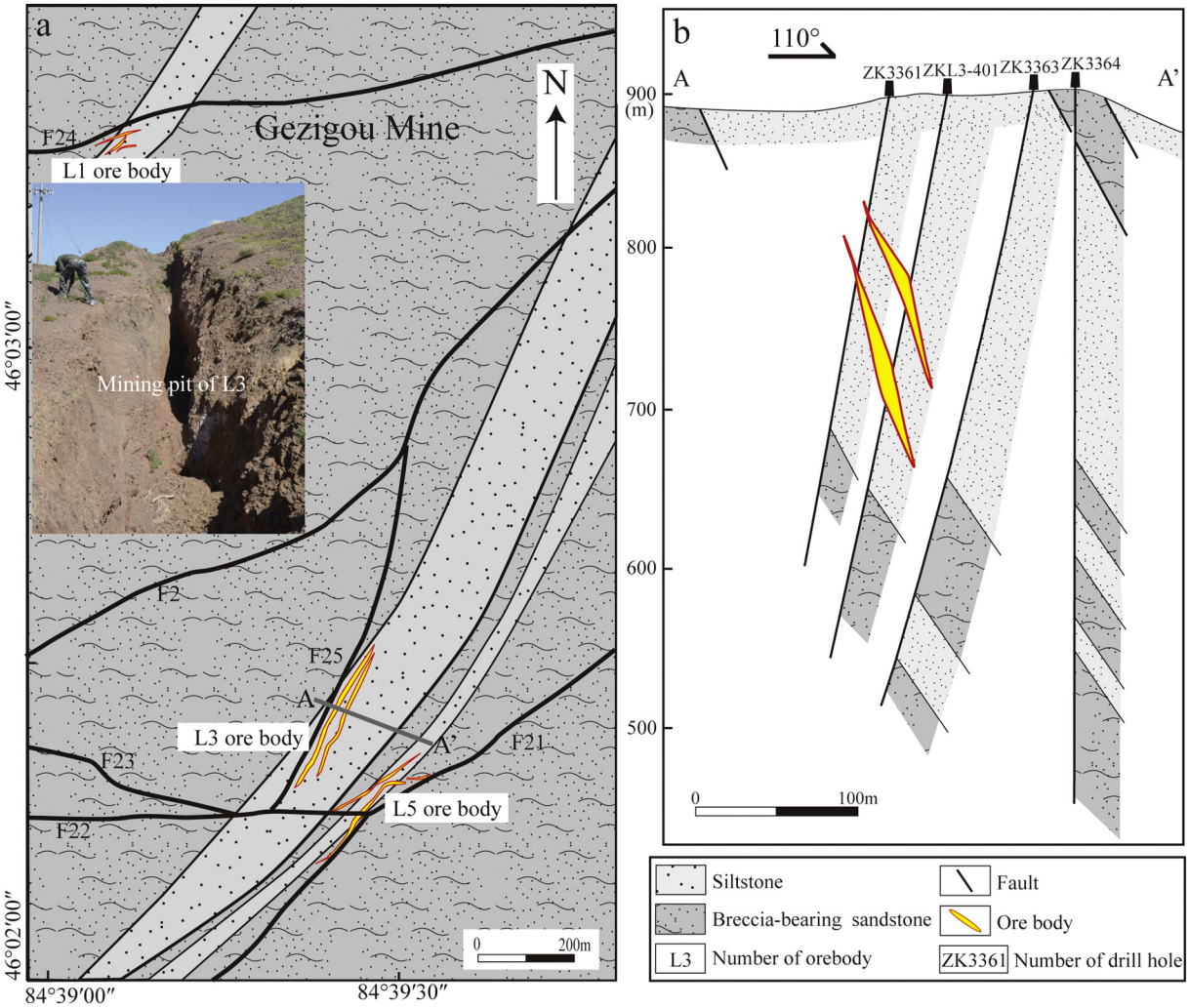

Fig. 2. (a) Geological map of the Gezigou gold deposit, showing the distribution of the ore bodies; the inserted photo shows the outcrop of the L3 ore body. (b) Geological cross section through the L3 ore body, modified after China National Gold Group Corporation Geology Co., Ltd. (2014).

Corporation Geology Co., Ltd, 2014). The geological characteristics and the types of L1, L3, and L5 ore bodies are similar. The L3 ore body was studied because it is the largest one among these ore bodies. The distribution of the L3 ore body is controlled by NE-NEE-striking faults. The varying thickness of the L3 ore body along the dip orientation is shown in drill sections (Fig. 2b).

4. Analytical methods

Forty representative samples from the L3 ore body were studied. The electron probe microanalysis of the minerals was conducted using a JEOL JXA-8230 electron microprobe at the Chinese Academy of Geological Sciences. The elements and X-ray lines used for this analysis were Fe (Kα), As (Lα), S (Kα), Pb (Mα), Ni (Kα), Ag (Lα), Cu (Kα), Zn (Kα), Co (Kα), Sb (Lα), and Au (Lα). The operating conditions included an accelerating voltage of 20 kV, a beam current of 10 nA, and an electron beam diameter of approximately 2 μm. The counting time was 10 s on the peak, 5 s on the low background position and 5 s on the high background position for each element. All of the standards (natural and synthetic) were tested for homogeneity before being utilized for quantitative analysis. The standard specimens are FeS_2 (Fe, S), CoAsS (Co, As), FeNiS (Ni), native silver (Ag), CuO (Cu), ZnS (Zn), TeSb (Sb), and native gold (Au). The ZAF correction method, consisting of atomic number correction (Z), absorption correction (A), and fluorescence correction (F), was used for standardization. The minimum detection limits of the sulfide minerals and native gold were Fe (176 ppm), As (232 ppm), S (71 ppm), Ni (152 ppm), Co (153 ppm), Bi (406 ppm), Zn (184 ppm), Cu (160 ppm), Ag (119 ppm), and Au (146 ppm).

Doubly polished thin section slabs were prepared for fluid inclusion microthermometry and laser Raman spectroscopy. The qualitative determination of single fluid inclusion composition was conducted using a Renishaw Invia Reflex Raman microspectrometer at Peking University. The laser wavelength was 532 nm, with a laser beam spot diameter of 1 μm and a spectrometer resolution of 1 cm^{-1}. Cooling and heating experiments were carried out using an INSTEC HCS622XY programmable heating-freezing stage attached to a Nikon ECLIPSE LV100POL transmitted light microscope at the Fluid Inclusion Lab of Peking University. Synthetic inclusions were used to test the accuracy of the calibration procedure. The estimated accuracy was ± 0.1 °C at temperatures below 100 °C and ± 1.0 °C at temperatures ranging from 100 to 600 °C. The heating/cooling rates were restricted to < 10 °C/min and decreased to 1 °C/min near phase transformations.

5. Results

5.1. Hydrothermal mineral paragenesis

Three types of hydrothermal veins are recognized in the L3 ore body: (1) quartz-sulfides veins; (2) arsenopyrite-calcite veins; and (3) quartz-calcite veins (Fig. 3). The quartz-sulfides veins, which have

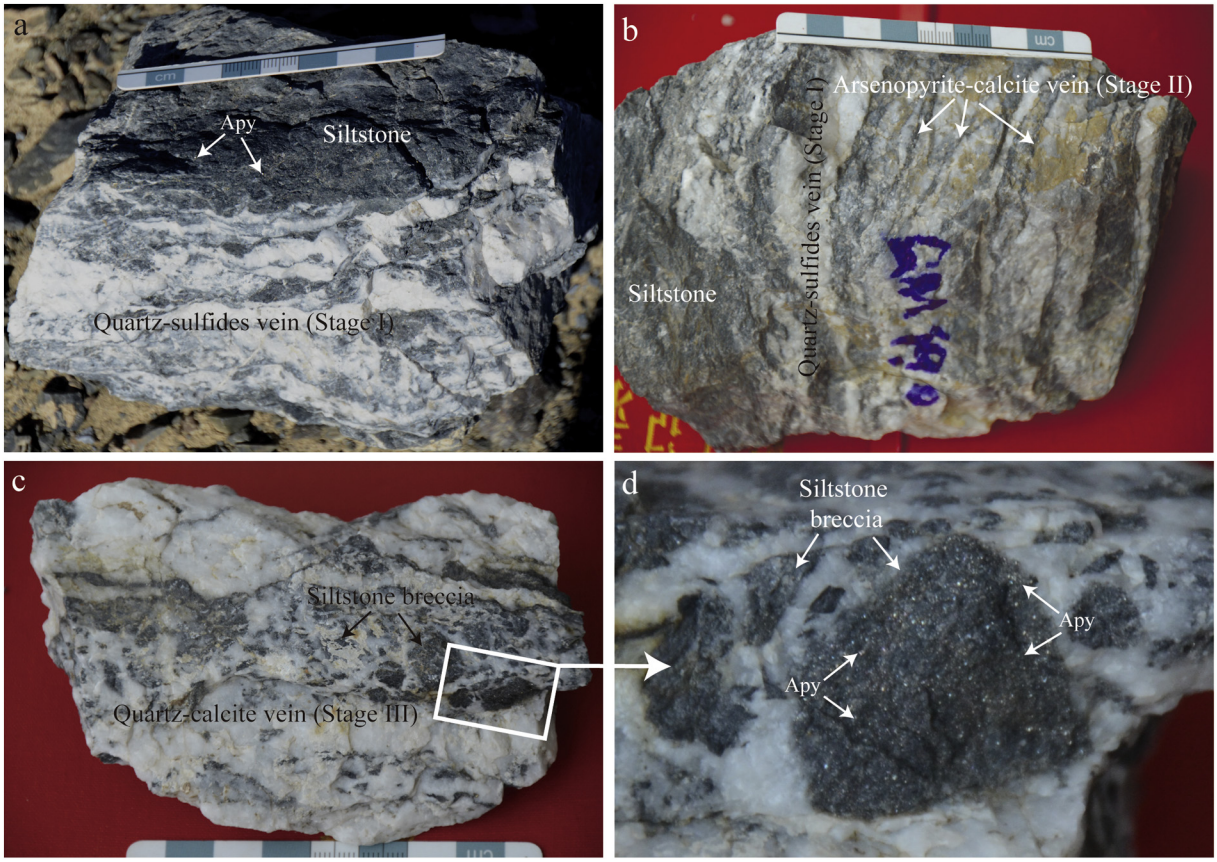

Fig. 3. Photographs showing ore samples from the Gezigou gold deposit. (a) Quartz-sulfides veins crosscut the mineralized siltstone. (b) Arsenopyrite-calcite veins crosscut a quartz-sulfides vein. (c) Numerous siltstone breccias were cemented by a quartz-calcite vein. (d) Many sulfides disseminated in the siltstone breccias.

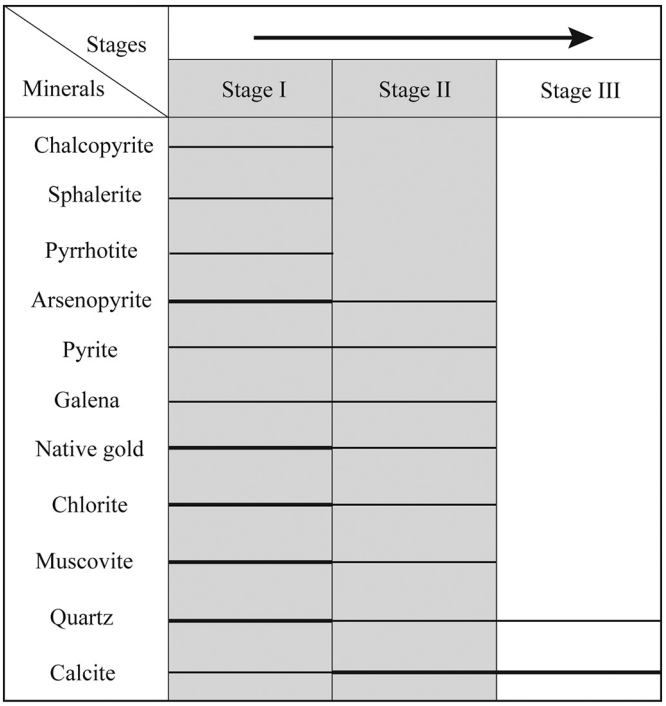

Fig. 4. The paragenetic sequence of minerals in the Gezigou gold deposit.

widths of 0.5–10 mm, represent the earliest hydrothermal event. Subsequently, the arsenopyrite-calcite veins, which have the widths of 0.1–1 mm, crosscut the quartz-sulfides veins. Finally, the quartz-calcite veins crosscut both the quartz-sulfides veins and arsenopyrite-calcite veins. Based on the different mineral textures, mineral assemblages and crosscutting relationships of these hydrothermal veins, three stages could be identified for the ore-forming process of the Gezigou gold deposit (Fig. 4): the quartz-sulfides-native gold stage (I), the arsenopyrite-calcite-native gold stage (II), and the quartz-calcite stage (III).

The quartz-sulfides-native gold stage (I) is represented by quartz-sulfides veins and disseminated sulfides in mineralized siltstone (Fig. 5a). Their mineral assemblage comprise quartz (40–50 vol%), calcite (10–20 vol%), muscovite (5–15 vol%), chlorite (5–10 vol%), sulfides (20–30 vol%), and native gold. The sulfides consist of coarse-grained arsenopyrite, pyrite, chalcopyrite, sphalerite, galena, and pyrrhotite. The graphite-bearing siltstone close to the quartz-sulfides veins also contains a number of disseminated sulfides (Fig. 5b, d). Arsenopyrite, which exhibits grain sizes of 0.2–1 mm and accounts for 70–80 vol% of all sulfides in the quartz-sulfides-native gold stage, contains inclusions of pyrite and sphalerite (Fig. 5c–d). Pyrite commonly occurs as anhedral crystal and coexists with arsenopyrite (Fig. 5c). Arsenopyrite is the only sulfide containing native gold, which mainly occurs as inclusions or fills microfractures in arsenopyrite (Fig. 5e–f). Some native gold grains with the grain size of 25 μm are associated with quartz (Fig. 5e). The graphite grains adjacent to the quartz-sulfides veins have generally been consumed by the quartz-sulfides veins (Fig. 5g), and some anhedral pyrite grains also occur in siltstone close to the quartz-sulfides veins (Fig. 5h).

The atomic percentage of As in the arsenopyrite in this stage is 29.5–31.0% (Table 1). Galena grains contain a certain amount of Se (0.95–1.07 wt%; Table 1). Native gold usually contains relatively high Ag contents (12.1–12.3 wt%; Table 1).

The arsenopyrite-calcite-native gold stage (II) is marked by arsenopyrite-calcite veins. The arsenopyrite-calcite veins, which crosscut

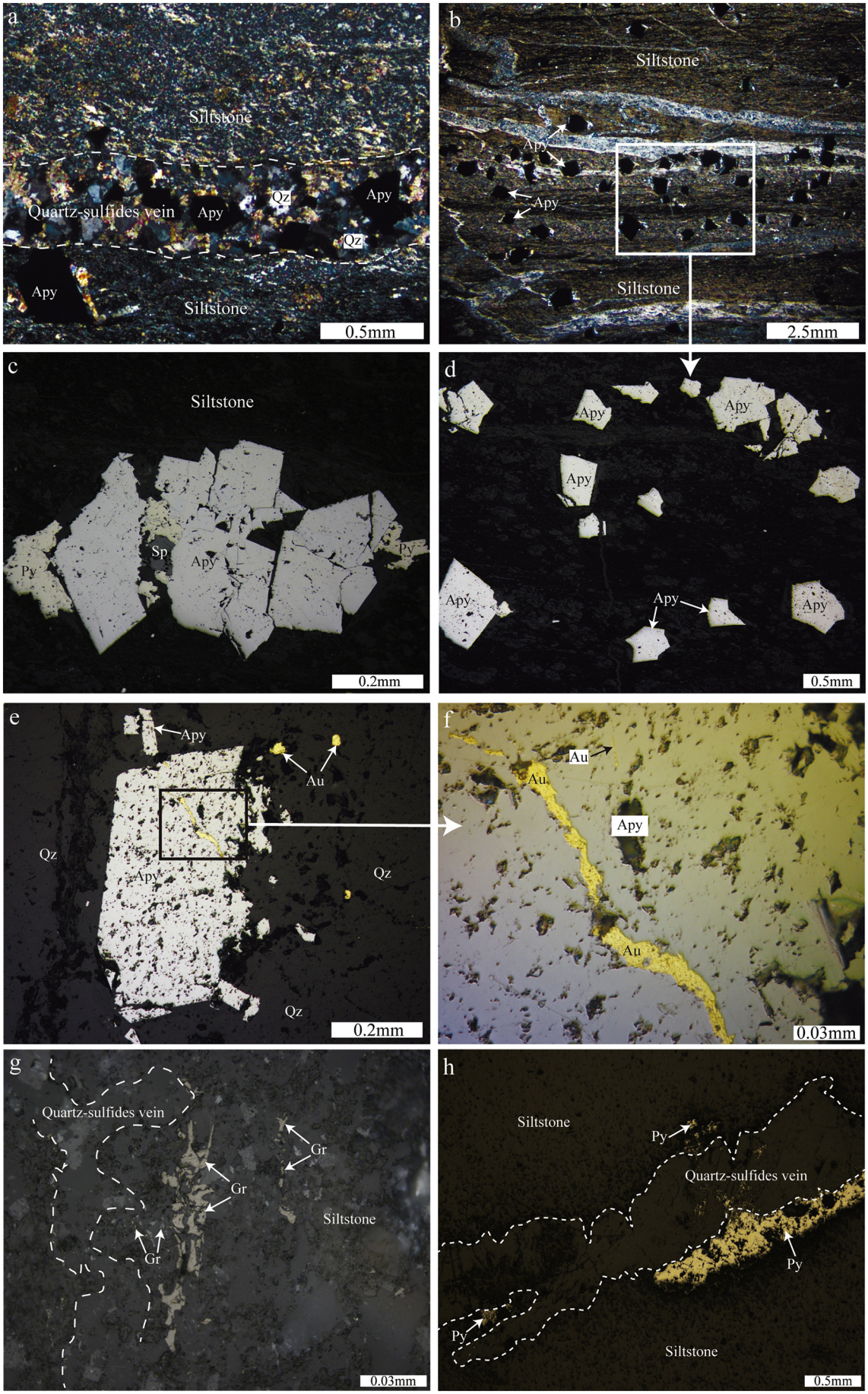

(caption on next page)

Fig. 5. Photomicrographs of the quartz-sulfides-native gold stage (I) in the Gezigou gold deposit. (a) Quartz-sulfides vein crosscuts the mineralized siltstone, cross-polarized light. (b, d) Abundant arsenopyrite grains disseminated in siltstone under (b) cross-polarized light and (d) reflected light. (c) Euhedral arsenopyrite coexists with pyrite and sphalerite, reflected light. (e–f) Native gold coexists with arsenopyrite, reflected light. (g) Several graphite grains adjacent to the quartz-sulfides vein that have been consumed by quartz-sulfides vein, reflected light. (h) Anhedral pyrite grains occur in siltstone close to the quartz-sulfides vein, reflected light. Apy - arsenopyrite, Au - native gold, Gr - graphite, Py - pyrite, Qz - quartz, and Sp - sphalerite.

the quartz-sulfides veins, consist of fine-grained arsenopyrite, calcite, quartz, pyrite, galena, and native gold (Fig. 6a–b). In contrast to stage I, calcite is the main gangue mineral in this stage. Arsenopyrite, which ranges in grain size from 20 μm to 0.2 mm, is the most abundant sulfide in the arsenopyrite-calcite-native gold stage (Fig. 6b–c). Galena is associated with arsenopyrite (Fig. 6d). Pyrite also locally coexists with arsenopyrite. Native gold grains occur in arsenopyrite as inclusions (Fig. 6d–e). The atomic percentage of As in the arsenopyrite in this stage is 28.8–30.1%, which is lower than that of the arsenopyrite in stage I (Table 1). Similar to that in stage I, the galena in this stage also contains a certain amount of Se (0.86–1.16 wt%; Table 1). The sphalerite in this stage contains lower Fe contents (5.92–6.50 wt%) than the sphalerite (7.03–8.19 wt%) in stage I (Table 1). The quartz-calcite stage (III) is marked by quartz-calcite veins, which are mainly composed of quartz and calcite. No native gold occurs in the quartz-calcite stage. A number of mineralized siltstone breccias, which contain disseminated sulfides and native gold (Fig. 3c–d), have been cemented by the quartz-calcite veins (Fig. 3c).

5.2. Fluid inclusions

5.2.1. Fluid inclusion types

Twenty-two doubly polished thin sections were made for petrological study, and of these thin sections, ten of them were selected for microthermometric and laser Raman analysis. The fluid inclusions within the *syn*-ore hydrothermal quartz of the quartz-sulfides-native gold stage (I) mostly occur in clusters and trails, and locally as isolated individual inclusions (Fig. 7a–b).

Isolated and clustered inclusions are recognized as primary inclusions, and the intergranular inclusions and the inclusions in trails are recognized as secondary inclusions based on Roedder's (1984) and Van Den Kerkhof and Hein's (2001) criteria. Gold-bearing arsenopyrite coexists with quartz closely in stage I, therefore only primary fluid inclusions within quartz can constrain the ore-forming environment (Fig. 7a, d). Three types of fluid inclusions in quartz from the quartz-sulfides-native gold stage (I) of the Gezigou gold deposit were identified based on their phase transitions upon heating and cooling, and laser Raman spectroscopic analysis. These fluid inclusions are characterized by the presence of vapor and liquid phases without halite crystals at room temperature. In the arsenopyrite-calcite-native gold stage (II) and quartz-calcite stage (III), calcite is the most abundant gangue mineral, and no fluid inclusions were found in calcite. The fluid inclusions within quartz in stage II and III are too small to yield accurate measurement data.

Three types of fluid inclusions were described and selected for microthermometric measurement. Type-1 is two-phase aqueous inclusions, which contain a relatively small bubble (< 50 vol%) at room temperature. They vary from 3 to 15 μm in size and typically show rounded or negative crystal shapes (Fig. 7b–c). The aqueous fluid inclusions are commonly scattered in the quartz as isolated inclusions. These inclusions all homogenized to the liquid phase during the heating process. Type-2 is two-phase CH_4-bearing aqueous inclusions consisting of aqueous liquid and a CH_4 bubble with an inconsistent phase ratio at room temperature. These inclusions vary from 3 to 12 μm in size and also show rounded or negative crystal shapes (Fig. 7d–e). Based on the mode of total homogenization, type-2 inclusions are subdivided into type-2a, which homogenize into a liquid phase, and type-2b, which homogenize into a vapor. Type-2 inclusions only show two phases (ice + CH_4 vapor) upon cooling but do show signs of CH_4 clathrate. Type-2a inclusions commonly coexist with type-2b inclusions in the same clusters (Fig. 7d–e). Type-3 is the secondary aqueous inclusions, which are distributed along secondary trails within stage-I quartz. They are 2 to 8 μm in diameter and their shapes vary from rounded to elongated and irregular (Fig. 7a–b, f). These inclusions all homogenized to the liquid phase during the heating, as well as type-1 inclusions.

Laser Raman spectroscopic analysis was carried out to reveal the liquid and vapor compositions of fluid inclusions. The liquid phases of these inclusions are almost solely H_2O. The vapor phases of type-1 and type-3 inclusions are also H_2O, and the vapor phases of type-2 inclusions are dominated by CH_4 with trace amounts of N_2 (Fig. 8). These features indicate that the ore-forming fluid is an H_2O-CH_4-NaCl system.

5.2.2. Microthermometry

The salinities of the type-1 and type-3 inclusions were calculated using the equation for the NaCl-H_2O system given by Bodnar (1993). The ice-melting temperature of the type-2b inclusions could not be measured because of the poor visibility for type-2b inclusions during phase transformation. The salinities of all inclusions are reported as wt % NaCl equiv.

The final ice-melting temperature for type-1 inclusion ranges from −2.1 to −1.7 °C, corresponding to low salinities from 2.9 to 3.6 wt% NaCl equiv. (Fig. 9a–b). The homogenization temperature ranges from 302 to 345 °C (Fig. 9a). The ice-melting temperature for type-2a inclusions varies from −3.2 to −2.1 °C, corresponding to salinities from 3.6 to 5.3 wt% NaCl equiv., and the dissociation temperature of CH_4 clathrate (Tm clathrate) ranges from 11.8 to 15.6 °C. These fluid inclusions homogenized into liquid upon heating with the homogenization temperature ranging from to 353 to 391 °C (Fig. 9a). Among the analyzed type-2b inclusions, all inclusions homogenized into vapor upon heating with the homogenization temperatures ranging from 364 to 392 °C (Fig. 9a). The Tm clathrate for type-2b ranges from 14.7 to 18.9 °C. Type-2a inclusions generally coexist with type-2b inclusions with the consistent homogenization temperatures (353–392 °C). Type-3 inclusions have the homogenization temperature ranging from 217 to 261 °C (Fig. 9a). The ice-melting temperatures of −1.9 to −0.9 °C were obtained, corresponding to salinities from 1.6 to 3.2 wt% NaCl equiv. (Fig. 9b).

For type-2 CH_4-bearing aqueous inclusions, CH_4 clathrate is stable at the ice-melting temperature and some portion of H_2O would exist in the clathrate phase. Therefore, the salinity calculated based on the ice-melting temperature will be higher than the actual salinity (Lin et al., 2007; Zhong et al., 2013). Consequently, the ore-forming fluid in quartz-sulfides-native gold stage (I) is characterized by its low salinity.

5.3. Thermodynamic modeling

The thermodynamic modeling of the Au-Cu-As-Fe-S system was carried out using the SUPCRT92 software package (Johnson et al., 1992) with the updated database of slop16.dat on the GEOPIG website (SUPCRT92 online interface, http://geopig3.la.asu.edu:8080/GEOPIG/pigopt1.html). The thermodynamic properties of arsenopyrite and $As(OH)_3$ are from Pokrovski et al. (2002a) and Perfetti et al. (2008), respectively. The applied equations are listed in Table 2. A phase diagram based on thermodynamic modeling is constructed to display the stability fields of various sulfides that formed in the Gezigou gold deposit and the solubility curves of $As(OH)_3$ and $Au(HS)_2^-$ (Fig. 10). This diagram is constructed for case at 370 °C (500 bar) corresponding to the ore-forming condition of stage I. The presence of abundant sulfides and

Table 1
Representative compositions of sulfides and native gold in the Gezigou gold deposit (in wt%).

Minerals	Stage	Ag	Fe	Co	Ni	Cu	Zn	Se	Au	S	Pb	Sb	Te	As	Total	As*
Apy1	I	b.l.	36.8	0.03	b.l.	0.02	b.l.	b.l.	0.08	21.5	0.02	0.01	b.l.	41.7	100.2	29.5
Apy1	I	b.l.	36.7	0.08	0.02	0.01	b.l.	b.l.	0.07	21.4	0.06	0.09	0.03	41.9	100.4	29.7
Apy1	I	b.l.	36.7	b.l.	0.01	0.04	b.l.	b.l.	0.10	21.3	0.03	b.l.	0.03	42.0	100.3	29.8
Apy1	I	b.l.	36.0	0.02	b.l.	b.l.	b.l.	b.l.	0.02	20.9	0.09	0.07	b.l.	43.2	100.4	30.8
Apy1	I	0.05	35.9	0.04	0.05	b.l.	b.l.	b.l.	b.l.	20.4	0.06	0.03	b.l.	43.1	99.6	31.0
Apy1	I	b.l.	35.6	0.22	0.25	b.l.	b.l.	b.l.	0.09	22.0	0.02	b.l.	b.l.	41.8	100.0	29.6
Apy1	I	0.01	36.0	b.l.	0.01	b.l.	b.l.	b.l.	0.04	21.7	0.06	0.32	b.l.	42.0	100.1	29.8
Apy1	I	b.l.	36.3	0.04	0.01	b.l.	0.05	b.l.	0.04	21.3	b.l.	0.06	0.04	42.3	100.2	30.0
Apy1	I	b.l.	37.0	0.05	0.04	b.l.	0.04	b.l.	b.l.	21.5	b.l.	0.09	b.l.	41.9	100.6	29.5
Apy1	I	b.l.	36.4	b.l.	b.l.	b.l.	0.04	b.l.	b.l.	20.6	0.06	0.01	b.l.	43.4	100.4	30.9
Apy1	I	b.l.	36.2	0.04	b.l.	b.l.	b.l.	b.l.	0.03	21.3	0.08	0.08	0.01	42.1	99.8	30.0
Apy1	I	0.04	36.4	0.06	0.18	b.l.	0.07	b.l.	0.04	21.7	0.03	0.04	b.l.	42.3	100.8	29.8
Apy2	II	b.l.	36.7	0.02	0.01	b.l.	b.l.	b.l.	b.l.	21.6	0.14	0.04	b.l.	42.1	100.6	29.6
Apy2	II	0.02	37.1	b.l.	b.l.	0.04	b.l.	b.l.	b.l.	21.2	b.l.	b.l.	0.04	41.9	100.3	29.7
Apy2	II	0.11	37.4	0.03	b.l.	b.l.	0.05	b.l.	0.10	22.2	0.06	b.l.	b.l.	41.3	101.2	28.8
Apy2	II	0.02	37.1	0.01	b.l.	b.l.	b.l.	b.l.	b.l.	21.4	b.l.	0.03	b.l.	41.2	99.8	29.2
Apy2	II	b.l.	36.7	0.06	b.l.	b.l.	b.l.	b.l.	0.04	21.3	0.03	0.20	b.l.	41.8	100.0	29.7
Apy2	II	b.l.	37.0	0.03	0.01	b.l.	0.02	b.l.	b.l.	21.5	b.l.	0.18	b.l.	41.4	100.1	29.3
Apy2	II	0.04	36.4	0.03	0.01	b.l.	b.l.	b.l.	b.l.	20.9	b.l.	0.08	0.01	42.0	99.4	30.1
Apy2	II	b.l.	36.5	0.03	b.l.	0.04	b.l.	b.l.	0.10	21.0	0.06	0.04	b.l.	41.5	99.2	29.8
Apy2	II	0.09	36.2	0.04	0.02	b.l.	b.l.	b.l.	0.03	21.0	0.01	0.09	b.l.	41.3	98.8	29.7
Apy2	II	0.03	36.9	0.04	b.l.	b.l.	b.l.	b.l.	0.03	21.5	0.05	0.11	b.l.	42.2	100.8	29.7
Pyrite	I	0.01	46.4	0.06	0.03	0.04	0.03	b.l.	0.07	52.8	0.10	b.l.	b.l.	0.02	99.5	
Pyrite	I	b.l.	47.5	b.l.	0.03	b.l.	b.l.	b.l.	b.l.	53.2	0.02	b.l.	b.l.	0.08	100.9	
Pyrite	I	b.l.	47.3	0.04	0.06	0.02	b.l.	0.05	0.02	52.9	b.l.	b.l.	b.l.	0.02	100.4	
Pyrite	I	b.l.	47.5	0.07	0.02	0.01	0.07	b.l.	b.l.	53.4	b.l.	0.02	b.l.	b.l.	101.1	
Pyrite	I	0.06	47.4	0.07	0.06	0.10	b.l.	0.01	0.05	52.6	0.03	b.l.	0.01	0.07	100.4	
Pyrite	I	b.l.	47.0	0.04	0.02	b.l.	b.l.	0.03	b.l.	52.2	0.10	0.06	0.02	b.l.	99.5	
Pyrite	I	0.06	46.9	0.07	0.10	0.01	0.08	0.03	0.08	52.6	b.l.	b.l.	0.02	0.26	100.2	
Pyrite	I	b.l.	47.3	0.01	b.l.	b.l.	0.05	0.01	b.l.	52.6	0.09	b.l.	0.03	b.l.	100.2	
Pyrite	I	b.l.	46.8	0.04	b.l.	0.04	0.05	b.l.	b.l.	53.0	b.l.	0.02	b.l.	b.l.	100.0	
Pyrite	I	b.l.	47.6	0.01	0.06	0.02	0.10	b.l.	b.l.	52.7	b.l.	b.l.	0.03	0.11	100.6	
Pyrite	I	b.l.	47.4	0.05	0.02	b.l.	b.l.	0.03	b.l.	52.5	b.l.	b.l.	b.l.	0.25	100.3	
Pyrite	I	b.l.	47.1	0.09	b.l.	b.l.	b.l.	0.01	0.03	53.1	0.01	0.01	b.l.	b.l.	100.4	
Pyrite	I	b.l.	47.2	0.04	0.04	0.02	0.02	0.03	0.01	53.3	0.02	0.01	0.06	0.13	100.9	
Pyrite	I	0.03	47.2	0.04	0.04	0.06	0.02	b.l.	b.l.	53.4	b.l.	b.l.	b.l.	b.l.	100.8	
Pyrite	II	b.l.	47.4	0.02	b.l.	b.l.	b.l.	b.l.	b.l.	52.4	0.15	0.03	b.l.	0.36	100.3	
Pyrite	II	b.l.	47.2	0.04	b.l.	b.l.	0.07	b.l.	0.04	53.2	0.05	0.02	b.l.	b.l.	100.6	
Pyrite	II	b.l.	47.4	0.05	b.l.	b.l.	0.02	b.l.	b.l.	53.0	0.06	b.l.	b.l.	0.06	100.6	
Pyrite	II	b.l.	47.6	0.06	0.03	b.l.	b.l.	0.07	0.05	52.9	b.l.	0.05	b.l.	b.l.	100.7	
Pyrite	II	b.l.	47.0	0.02	b.l.	0.04	0.03	0.01	b.l.	52.7	0.03	b.l.	b.l.	b.l.	99.8	
Pyrite	II	0.01	47.5	0.07	b.l.	b.l.	b.l.	0.03	0.01	52.7	0.08	b.l.	b.l.	0.34	100.8	
Pyrite	II	0.03	47.3	0.05	b.l.	0.02	0.02	0.02	b.l.	53.2	0.04	b.l.	b.l.	0.24	100.9	
Pyrite	II	b.l.	47.1	0.01	b.l.	0.28	b.l.	b.l.	b.l.	52.8	0.05	b.l.	b.l.	0.02	100.3	
Pyrite	II	0.06	46.4	0.02	b.l.	b.l.	b.l.	b.l.	b.l.	52.8	0.03	b.l.	b.l.	b.l.	99.3	
Pyrite	II	0.03	46.7	0.05	b.l.	b.l.	0.01	b.l.	b.l.	52.8	0.03	0.12	b.l.	0.13	99.8	
Pyrite	II	b.l.	47.2	0.03	b.l.	0.01	b.l.	0.02	0.06	52.3	0.06	b.l.	0.01	0.04	99.8	
Sphalerite	I	b.l.	7.39	b.l.	0.04	b.l.	58.2	b.l.	0.07	33.2	b.l.	0.03	b.l.	b.l.	98.9	
Sphalerite	I	b.l.	8.19	0.03	b.l.	b.l.	56.1	0.11	b.l.	32.8	0.11	b.l.	0.02	b.l.	97.3	
Sphalerite	I	b.l.	7.95	0.04	0.05	b.l.	56.5	0.04	0.06	33.0	b.l.	0.02	b.l.	b.l.	97.7	
Sphalerite	I	b.l.	7.03	b.l.	b.l.	b.l.	57.8	b.l.	b.l.	32.9	b.l.	b.l.	0.01	0.01	97.7	
Sphalerite	I	b.l.	7.91	0.05	b.l.	b.l.	55.7	0.03	b.l.	32.9	0.06	b.l.	b.l.	0.01	96.7	
Sphalerite	I	b.l.	7.94	0.01	b.l.	b.l.	56.9	b.l.	b.l.	33.2	b.l.	b.l.	0.05	b.l.	98.0	
Sphalerite	I	b.l.	7.51	b.l.	b.l.	b.l.	58.1	b.l.	0.04	33.0	0.06	b.l.	b.l.	b.l.	98.8	
Sphalerite	II	b.l.	5.92	0.01	b.l.	0.47	58.9	b.l.	b.l.	32.8	b.l.	b.l.	b.l.	b.l.	98.1	
Sphalerite	II	b.l.	6.23	0.02	b.l.	b.l.	58.3	b.l.	b.l.	33.4	0.01	b.l.	b.l.	0.09	98.0	
Sphalerite	II	b.l.	6.50	0.02	b.l.	0.24	58.8	0.02	0.02	33.2	0.08	b.l.	b.l.	b.l.	98.9	
Sphalerite	II	b.l.	6.45	0.02	b.l.	0.02	58.9	0.06	b.l.	33.2	0.04	b.l.	b.l.	b.l.	98.7	
Galena	I	b.l.	b.l.	0.03	b.l.	b.l.	0.03	0.95	b.l.	13.0	87.3	b.l.	0.05	b.l.	101.4	
Galena	I	0.06	0.03	b.l.	b.l.	b.l.	b.l.	1.07	b.l.	12.7	86.8	b.l.	0.05	b.l.	100.7	
Galena	I	0.06	0.10	0.03	b.l.	b.l.	0.03	1.06	b.l.	12.8	86.0	b.l.	0.16	b.l.	100.3	
Galena	I	b.l.	0.38	b.l.	b.l.	b.l.	b.l.	0.95	b.l.	12.6	85.7	b.l.	0.06	b.l.	99.7	
Galena	II	0.02	b.l.	b.l.	0.03	b.l.	0.01	0.86	b.l.	12.9	86.8	0.06	0.08	b.l.	100.8	
Galena	II	b.l.	0.07	0.01	b.l.	b.l.	b.l.	0.91	b.l.	12.9	85.0	b.l.	0.02	b.l.	98.8	
Galena	II	b.l.	0.15	0.01	0.06	0.10	b.l.	0.94	b.l.	13.0	88.4	b.l.	b.l.	b.l.	102.7	
Galena	II	b.l.	0.58	0.01	b.l.	b.l.	b.l.	0.95	b.l.	12.8	87.0	b.l.	0.09	b.l.	101.4	
Galena	II	b.l.	0.89	b.l.	b.l.	0.04	0.05	1.16	b.l.	12.3	84.5	b.l.	0.06	b.l.	99.0	
Galena	II	b.l.	0.47	0.04	b.l.	b.l.	b.l.	1.13	b.l.	12.8	86.8	0.03	0.05	b.l.	101.3	
Chalcopyrite	I	0.04	30.5	0.04	b.l.	34.6	0.25	0.01	b.l.	34.9	b.l.	b.l.	0.02	b.l.	100.3	
Chalcopyrite	I	0.03	30.2	0.03	0.03	34.2	0.10	0.03	b.l.	35.3	0.02	b.l.	b.l.	b.l.	99.9	
Chalcopyrite	I	0.04	30.2	0.04	b.l.	34.3	b.l.	0.02	0.03	34.7	0.12	b.l.	b.l.	b.l.	99.5	
Native gold	I	12.2	0.02	0.02	b.l.	b.l.	b.l.	0.01	88.7	0.03	b.l.	b.l.	0.15	b.l.	101.1	
Native gold	I	12.2	b.l.	b.l.	0.04	b.l.	b.l.	b.l.	87.2	0.01	b.l.	b.l.	b.l.	b.l.	99.5	
Native gold	I	12.1	0.03	0.01	0.02	b.l.	b.l.	b.l.	87.8	b.l.	b.l.	0.01	0.05	0.03	100.0	

(*continued on next page*)

Table 1 (*continued*)

Minerals	Stage	Ag	Fe	Co	Ni	Cu	Zn	Se	Au	S	Pb	Sb	Te	As	Total	As*
Native gold	I	12.3	0.02	b.l.	0.02	b.l.	b.l.	b.l.	88.0	b.l.	b.l.	b.l.	b.l.	0.02	100.3	

As* = Atomic percent (at.%) of As in arsenopyrite. b.l. = below the detection limit. Apy1 = arsenopyrite in stage I, Apy2 = arsenopyrite in stage II.

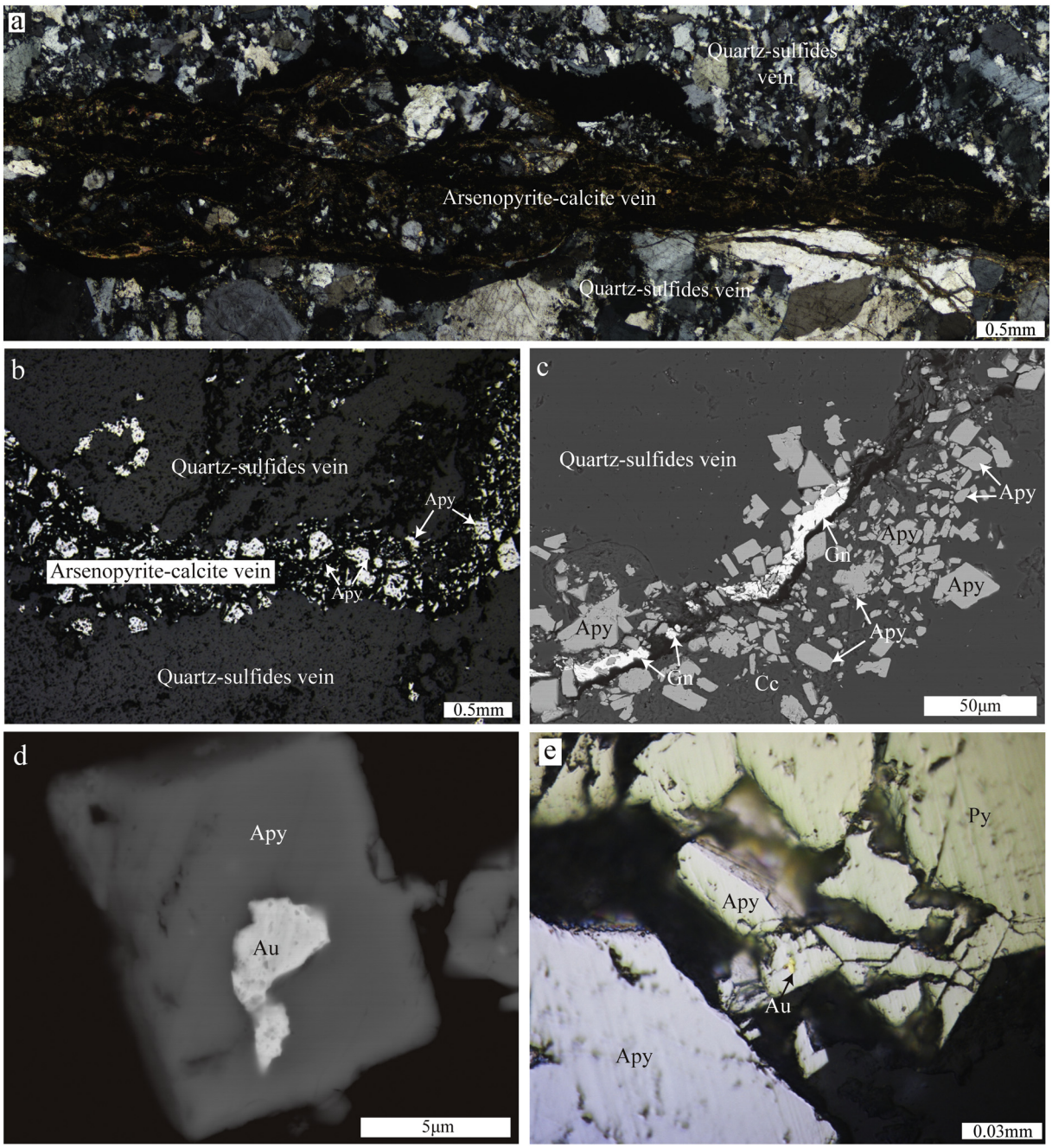

Fig. 6. Photomicrographs of the arsenopyrite-calcite-native gold stage (II) in the Gezigou gold deposit. (a) Quartz-sulfides vein was crosscut by an arsenopyrite-calcite vein, cross-polarized light. (b) Arsenopyrite-calcite vein mainly consists of fine-grained arsenopyrite and calcite, reflected light. (c) Arsenopyrite coexists with galena and calcite, BSE. (d–e) Native gold grains in arsenopyrite (d) BSE and (e) reflected light. Apy - arsenopyrite, Au - native gold, Cc - calcite, Gn - galena, and Py - pyrite.

the absence of sulfate indicate that H_2S is the main form of sulfur in the ore-forming fluid. Therefore, a_{H2S} is used as the vertical coordinate.

6. Discussion

6.1. T-P-fS_2-pH constraints of the ore-forming fluid

The deposition of metals to form an ore deposit occurs in response to physico-chemical changes. Changes in physico-chemical conditions

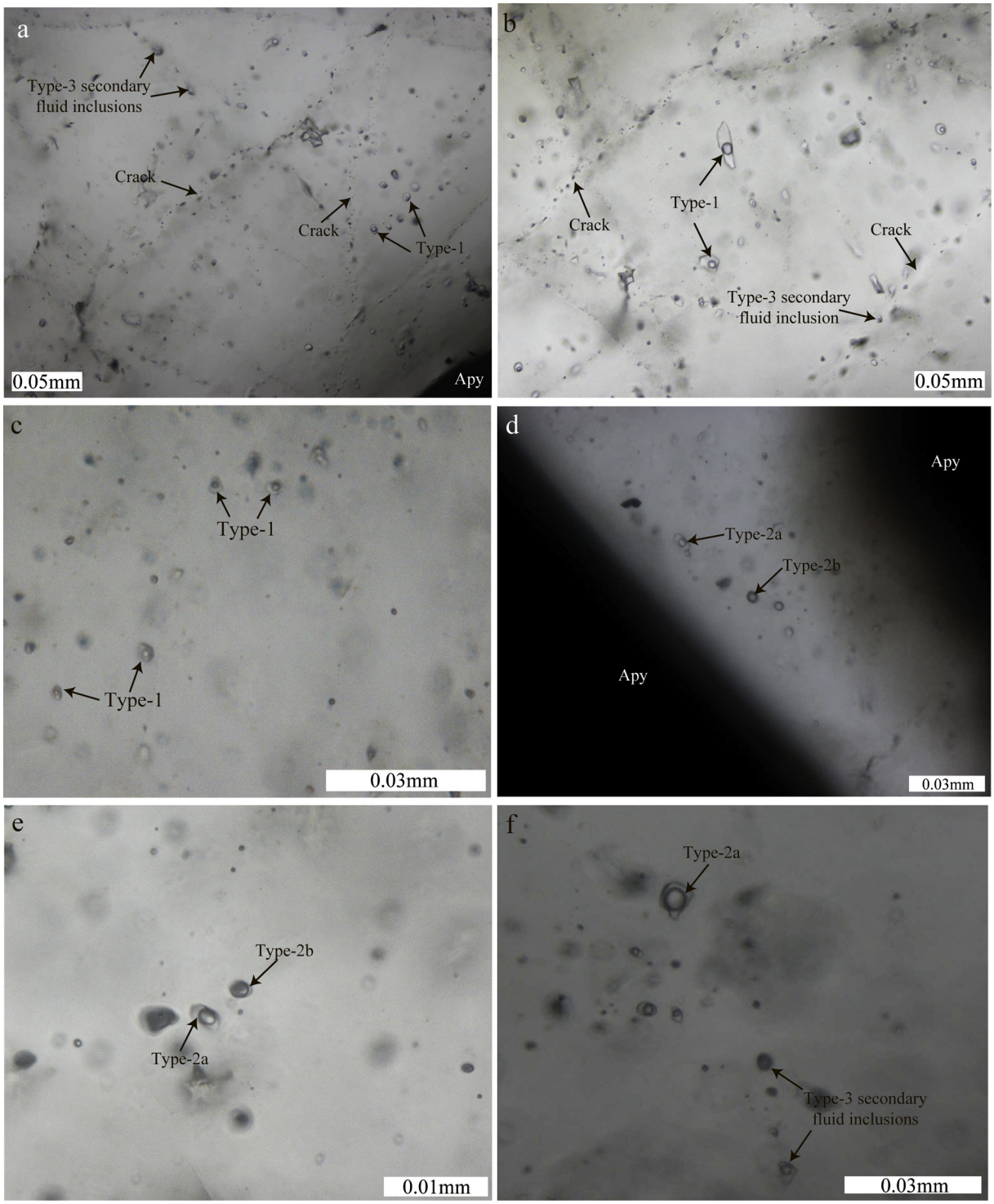

Fig. 7. Photomicrographs of representative fluid inclusions in the quartz-sulfides-native gold stage. (a–b) Isolated primary fluid inclusions and secondary fluid inclusions located in a crack within quartz. (c) Type-1 aqueous inclusions in quartz. (d) Type-2 CH_4-bearing aqueous inclusions in quartz, which coexists with arsenopyrite closely. (e) Coexistence of type-2a and type-2b fluid inclusions in quartz. (f) Type-3 secondary inclusions in the trail. Apy – arsenopyrite.

such as temperature, pressure, oxygen fugacity, and sulfur fugacity are effective mechanisms for gold precipitation (Zhu and An, 2010; Seward et al., 2014). Temperature can be used to estimate the migrating form of gold, the ore-forming process, and the type of gold deposit. As mentioned above, type-2a inclusions generally coexist with type-2b inclusions in stage I with the different mode of homogenization and consistent homogenization temperatures, which indicates phase separation and the generation of fluid inclusions by heterogeneous trapping during stage I. The microthermometric measurements show that the homogenization temperatures of coexisting type-2a and type-2b inclusions range from 353 to 392 °C (Fig. 9a), which represent the exact trapping temperature because of the occurrence of phase separation (Roedder, 1984). The crystallization temperature of arsenopyrite can also be obtained by arsenopyrite geothermometer based on the atomic percentage of As in arsenopyrite (Kretschmar and Scott, 1976; Sharp et al., 1985). Our calculated results show that the formation temperatures of

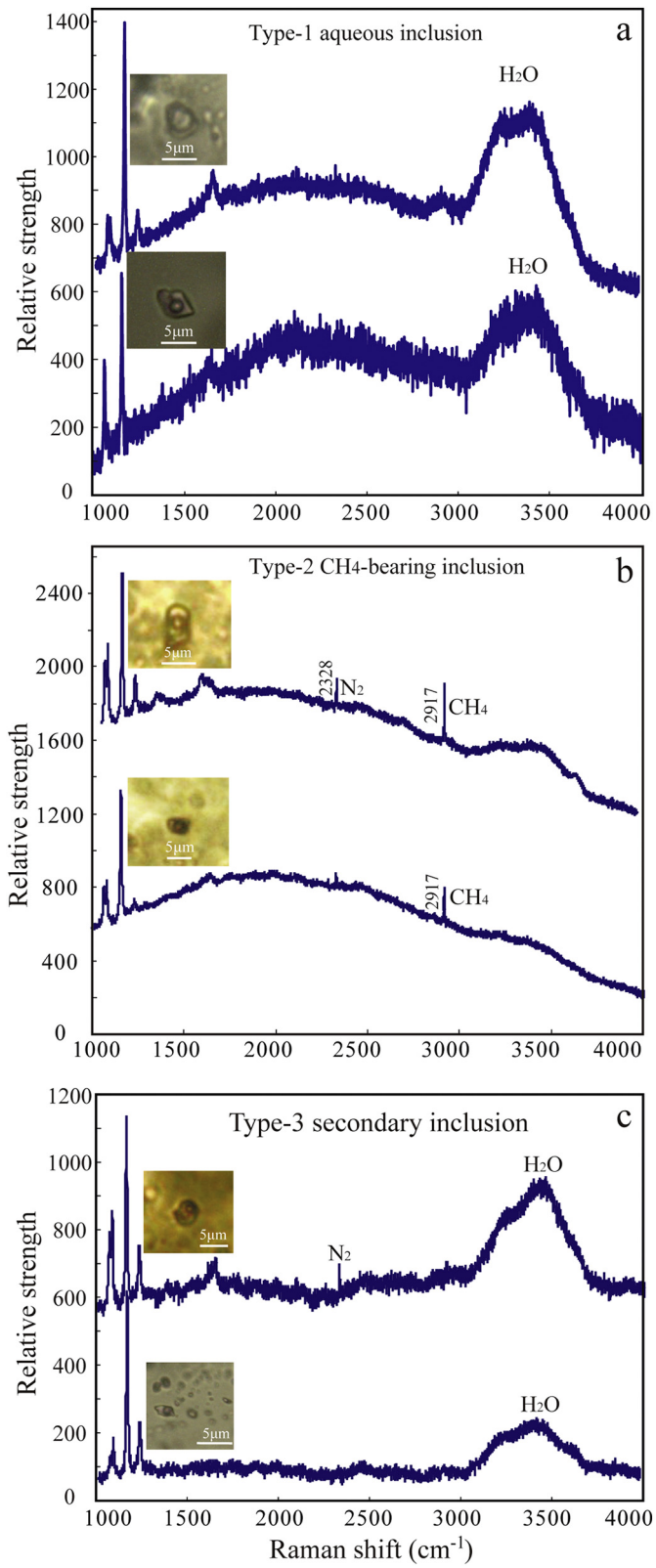

Fig. 8. Laser Raman spectra of three types of fluid inclusions in the quartz-sulfides-native gold stage.

arsenopyrites in stages I and II are 297–370 °C and 276–320 °C, respectively (Fig. 11). This temperature obtained for stage I is approximately consistent with the trapping temperature of type-2a and type-2b inclusions (353–392 °C).

As mentioned above, the salinities of type-2a and type-2b inclusions are very low. Therefore, type-2 inclusions can be regarded as an approximation of the H_2O-CH_4 system. The pressure estimation for type-2a and type-2b inclusions in stage I can be calculated using the online calculation program of the Zhenhao Duan Research Group (accessible at http://calc.geochemmodel.org/Pages/BinaryComposition.aspx) and the equations of state of Duan and Mao (2006) and Mao et al. (2009, 2010). The homogenization temperature, mode of homogenization, the dissociation temperature of CH_4 clathrate, and volume percentage of the vapor phase at 20 °C are required for calculation. The calculated result show the pressure estimated for type-2 inclusions is 264–833 bar. Therefore, the P-T conditions of quartz-sulfides-native stage (I) can be more precisely constrained as 353–392 °C and 264–833 bar.

In the quartz-sulfides-native gold stage (I), the homogenization temperature of type-1 inclusions is significantly lower than type-2a and type-2b inclusions (Fig. 9a). The most reasonable explanation accounting for the lower homogenization temperature of type-1 inclusions is the necessity for a pressure correction, which can only be applied to H_2O-NaCl inclusions (Potter, 1977). Except in the case of boiling systems, the homogenization temperature of fluid inclusions is lower than the trapping temperature, and therefore the homogenization temperatures of type-1 inclusions cannot represent the ore-forming temperature of stage I. On the other hand, the pressure-corrected temperatures of type-1 inclusions can constrain the ore-forming temperature of stage I. The pressure correction was made using Potter's (1977) diagram at 5.0 wt% NaCl and 500 bar. The obtained pressure-corrected temperature of type-1 inclusions is 342–390 °C, which is similar to the trapping temperature of type-2a and type-2b inclusions (353 to 392 °C).

The $\log fS_2$ values of the ore-forming system can be estimated using the arsenopyrite geothermometer diagram based on the mineral assemblage and temperature (Fig. 11; Kretschmar and Scott, 1976; Sharp et al., 1985). The results show that the $\log fS_2$ values decrease significantly from stages I to II (− 7.4 to −10.7 for stage I and − 9.2 to −12.0 for stage II). The pH value is also a significant parameter of the ore-forming system, as it can constrain the mineral assemblage and the migrating form of metal elements. Several silicate and carbonate minerals can be used to estimate the pH value of the ore-forming system. The equations involving K-feldspar, muscovite, and calcite can be written as follows (Hezarkhani et al., 1999; Seward et al., 2014):

$$KAl_2(Si_3AlO_{10})(OH)_{2muscovite} + 2\,K^+ + 6SiO_{2quartz} = 3KAlSi_3O_{8K-feldspar} + 2H^+ \quad (1)$$

$$CaCO_{3calcite} + 2H^+ = Ca^{2+} + CO_2 + H_2O \quad (2)$$

As shown in Eq. (1), at a higher pH, the stability of muscovite decreases, whereas K-feldspar may be the main K-bearing mineral. In contrast, at a lower pH, calcite will become unstable, as indicated by Eq. (2). According to these reactions, the presence of the mineral assemblage of muscovite, quartz, and calcite without K-feldspar in stages I and II of Gezigou gold deposit suggests that the pH of the ore-forming system was nearly neutral.

6.2. Mechanism of gold mineralization

Previous studies have suggested that gold hydrosulfide complexes (AuHS, $Au(HS)_2^-$) are the most dominant migrating form of Au at medium-low temperatures (Seward, 1973; Stefánsson and Seward, 2004). In high temperature, sulfur-saturated and reduced systems, gold is also transported as hydrosulfide complexes (Pokrovski et al., 2014; Zhong et al., 2015). AuHS is stable in acidic environments, whereas $Au(HS)_2^-$ is stable under weakly acidic to neutral conditions. $Au(HS)_2^-$ is the predominant ligand capable of carrying Au in the Gezigou gold deposit based on the estimated temperature, pH value, and redox conditions. The breakdown of $Au(HS)_2^-$ can result in gold deposition, as shown in the following reaction:

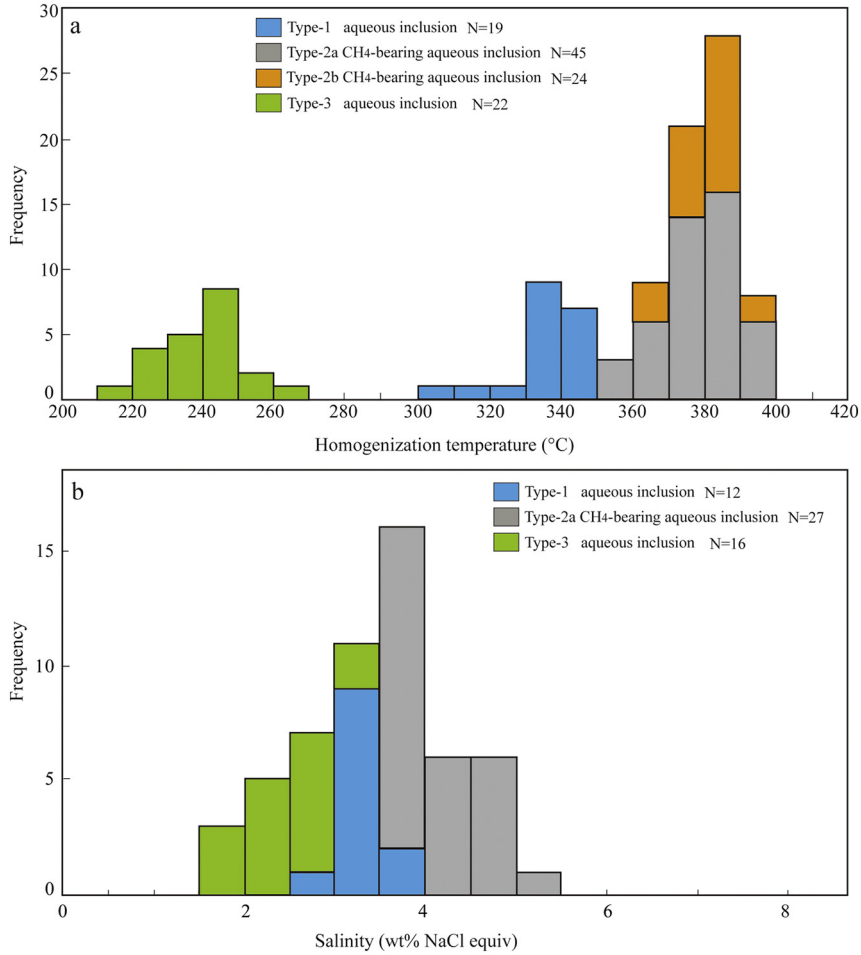

Fig. 9. Homogenization temperature (a) and salinity (b) histograms for three types of fluid inclusions in the quartz-sulfides-native gold stage.

Table 2
Summary of equations applied in the thermodynamic modeling of the Gezigou gold deposit.

$FeS_2 + H_2O = FeS + H_2S(aq) + 0.5O_2(g)$
$Fe_3O_4 + 3H_2S(aq) = 3FeS + 0.5O_2(g) + 3H_2O$
$Fe_3O_4 + 6H_2S(aq) + O_2(g) = 3FeS_2 + 6H_2O$
$4Fe_3O_4 + O_2(g) = 6Fe_2O_3$
$5CuFeS_2 + 6H_2O = Cu_5FeS_4 + 2Fe_2O_3 + 6H_2S(aq)$
$5CuFeS_2 + 2H_2S(aq) + O_2(g) = Cu_5FeS_4 + 4FeS_2 + 2H_2O$
$5CuFeS_2 + 2H_2O = Cu_5FeS_4 + 4FeS + 2H_2S(aq) + O_2(g)$
$15CuFeS_2 + 18H_2O = 3Cu_5FeS_4 + 4Fe_3O_4 + 18H_2S(aq) + O_2(g)$
$Au(HS)_2^- + 0.5H_2O = Au + H_2S(aq) + HS^-(aq) + 0.25O_2(g)$
$FeAsS + H_2S(aq) + 1.25O_2(g) + 0.5H_2O = FeS_2 + As(OH)_3(aq)$

These equations are from Benning and Seward (1996), Mikucki (1998), and Pokrovski et al. (2002a).

$$Au(HS)_2^- + 0.5H_2O \rightleftharpoons Au^0_{\text{native gold}} + H_2S + HS^- + 0.25O_2 \quad (3)$$

Although the temperature of the ore-forming system gradually decreases from stage I to stage II according to the result of the arsenopyrite geothermometer, cooling is not a direct cause of gold precipitation in the Gezigou gold deposit. With decreasing temperature, the solubility of $Au(HS)_2^-$ may actually increase due to its increased stability (Mikucki, 1998; Williams-Jones et al., 2009; Pokrovski et al., 2014). The ore-forming fluid with a high sulfur fugacity can even maintain high gold concentrations down to a temperature as low as 150 °C (Heinrich, 2005). Phase separation is a common mechanism for gold precipitation in hydrothermal deposits (Simmons et al., 2000; Williams-Jones and Heinrich, 2005), as H_2S strongly participates in the vapor phase during phase separation. As shown in Eq. (3), decreases in fS_2 will lead to gold precipitation. The fluid inclusion analysis of the Gezigou gold deposit shows that phase separation occurred in the quartz-sulfides-native gold stage (I). Phase separation triggered a decrease in fS_2, as evidenced by the change in the logfS_2 values estimated using the arsenopyrite geothermometer diagram (Fig. 11). In addition, ore-forming fluid reacting with graphite and iron-bearing matter in siltstone during fluid-rock reaction led to lower in fO_2 andfS_2 (Fig. 5g–h). Therefore, the gold deposition occurring in stage I in the Gezigou gold deposit may have been triggered by a decrease in fS_2 and fO_2 according to Eq. (3). In the arsenopyrite-calcite-native gold stage (II), native gold mainly occurs in arsenopyrite as inclusions. Arsenopyrite-calcite veins are generally thin and are not in contact with graphite-bearing siltstone, thus, phase separation and fluid-rock reaction were not the main factors causing native gold precipitation in stage II. Temperature can control the solubility of sulfides including pyrite and arsenopyrite (Seward et al., 2014), and a decrease in temperature will lead to sulfides crystallization. The decrease in fS_2 in the ore-forming fluid due to the arsenopyrite crystallization may be the key mechanism of gold precipitation in stage II.

The As(III) hydroxide complex ($As(OH)_3$) is the most dominant As-bearing species in natural hydrothermal systems over a wide range of temperatures (25 to 500 °C) and fluid densities (0.05 to 1.1 g cm^{-3}, Pokrovski et al., 1996, 2002a, 2002b; Perfetti et al., 2008). The most common As-bearing minerals found in low-temperature hydrothermal systems are orpiment (As_2S_3) and realgar (AsS) (Ballantyne and Moore, 1988; Eary, 1992). In high-temperature (T > 200 °C) geothermal systems, arsenopyrite and pyrite are the dominant As-bearing minerals (Ballantyne and Moore, 1988; Pokrovski et al., 2002a). The arsenic concentration in a solution in equilibrium with arsenopyrite can be

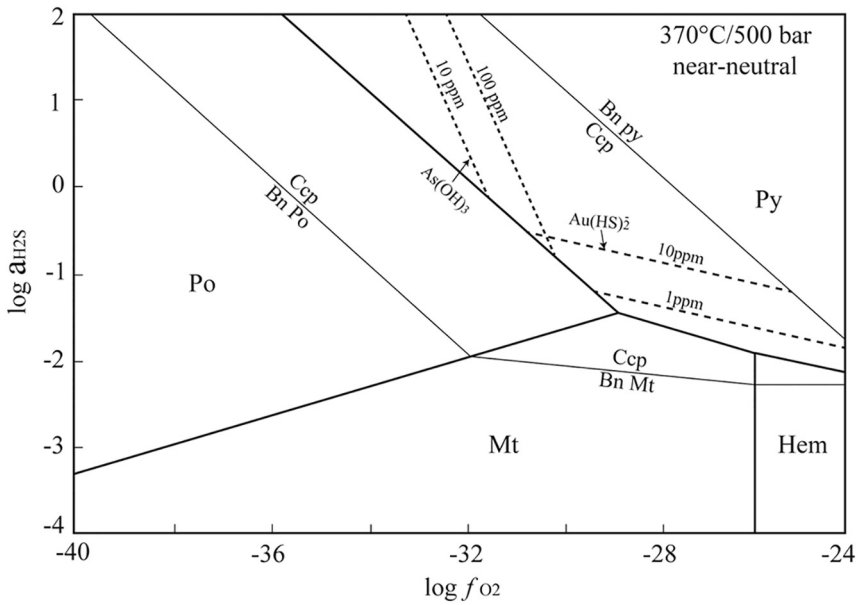

Fig. 10. Phase diagrams for the Au-Cu-As-Fe-S system in the Gezigou gold deposit. Bold lines show the stability fields of Fe-S-O minerals and thin lines show the stability fields of Cu-Fe-S minerals. Thin dotted lines represent the solubilities contours of $As(OH)_3$ and $Au(HS)_2^-$. The thermodynamic properties for arsenopyrite and $As(OH)_3$ are from Pokrovski et al. (2002a) and Perfetti et al. (2008), respectively. Other data are from the updated slop16.dat database of the SUPCRT92 software package.

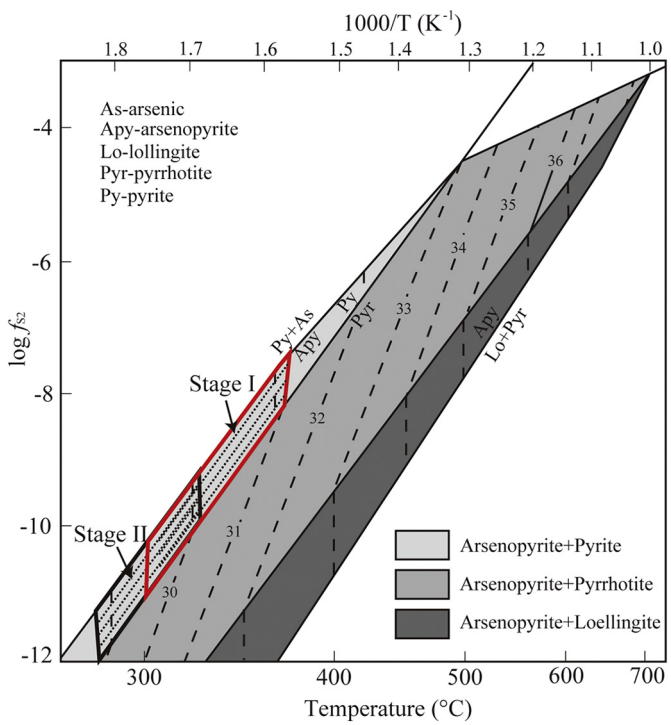

Fig. 11. Formation temperatures of arsenopyrites in the Gezigou gold deposit based on the atomic percentage of As in arsenopyrite by EPMA. Modified after Kretschmar and Scott (1976) and Sharp et al. (1985).

calculated by the iron conserving equilibrium reaction between arsenopyrite and pyrite (Heinrich and Eadington, 1986; Ballantyne and Moore, 1988; Pokrovski et al., 2002a):

$$FeAsS + H_2S + 1.25O_2 + 0.5H_2O = FeS_2 + As(OH)_3 \quad (4)$$

The main As-bearing mineral in the Gezigou gold deposit is arsenopyrite, which indicates that the ore-forming system is relatively reductive and rich in arsenic based on Eq. (4). The type-2a and type-2b inclusions both contain CH_4, which also suggests that the ore-forming system is reductive. According to Eq. (4), the content of $As(OH)_3$ in the hydrothermal system is also controlled by fS_2 and fO_2. Decreases in fS_2 and fO_2 can reduce the content of $As(OH)_3$ and enhance arsenopyrite crystallization. As mentioned above, gold deposition in the Gezigou gold deposit was also triggered by decreases in fS_2 and fO_2. A similar precipitation mechanism may be responsible for the coexistence of arsenopyrite and native gold (Fig. 5e–f), as indicated by the results of thermodynamic modeling (Fig. 10). Decreases in a_{H2S} and fO_2 could have reduced the solubilities of $As(OH)_3$ and $Au(HS)_2^-$ (Fig. 10) and consequently resulted in the precipitation of arsenopyrite and native gold.

6.3. Comparison with other gold deposits in west Junggar and a genetic model

The Gezigou, Huilvshan, and Mandongshan gold deposits, which are located in the Huilvshan-Mandongshan gold district, have similar ore types and are controlled by secondary faults related to the Anqi fault system.

The Huilvshan gold deposit is hosted in altered basalt and quartz-siderite rocks in a shear zone (Zhang and Zhu, 2016). Graphite-bearing sedimentary rocks are the main wall rocks of the Mandongshan and Gezigou gold deposits. The temperatures (~360–400 °C) of gold mineralization in the Mandongshan and Gezigou gold deposits are higher than those in the Huilvshan gold deposit (244–326 °C; Zhang and Zhu, 2016, 2017). Pyrite (40–60 vol%) is the most abundant sulfide in the Huilvshan gold deposit, and the native gold is mostly hosted by pyrite. Arsenopyrite (70–80 vol%) is the main sulfide in the Mandongshan and Gezigou gold deposits, and most of the native gold grains occur within arsenopyrite. The ore-forming fluid in the Huilvshan gold deposit is a CO_2-bearing aqueous solution, whereas the ore-forming fluids of the Mandongshan and Gezigou gold deposits are a CH_4-bearing aqueous solution. Such characteristics are typical of all gold deposits distributed along the Anqi fault in west Junggar. Pyrite is the dominant sulfide in the Hatu and Qi-III gold deposits, in which the fluid inclusions are rich in CO_2 (Wang and Zhu, 2015; Shen et al., 2016). Arsenopyrite is the major sulfide in the Baobei gold deposit (Wang and Zhu, 2007), in which the fluid inclusions are rich in CH_4 (Xie, 2009). This phenomenon suggests that the relative contents of these sulfides are controlled by the redox conditions of the ore-forming system. This can also be explained by Eq. (4), where a decrease in fO_2 facilitates the precipitation of arsenopyrite instead of pyrite. The Baogutu copper deposit is also characterized by CH_4-rich hydrothermal fluid in west Junggar and it is categorized as a reduced porphyry copper deposit (Shen et al., 2010; Cao et al., 2014). However, the mineral assemblage and

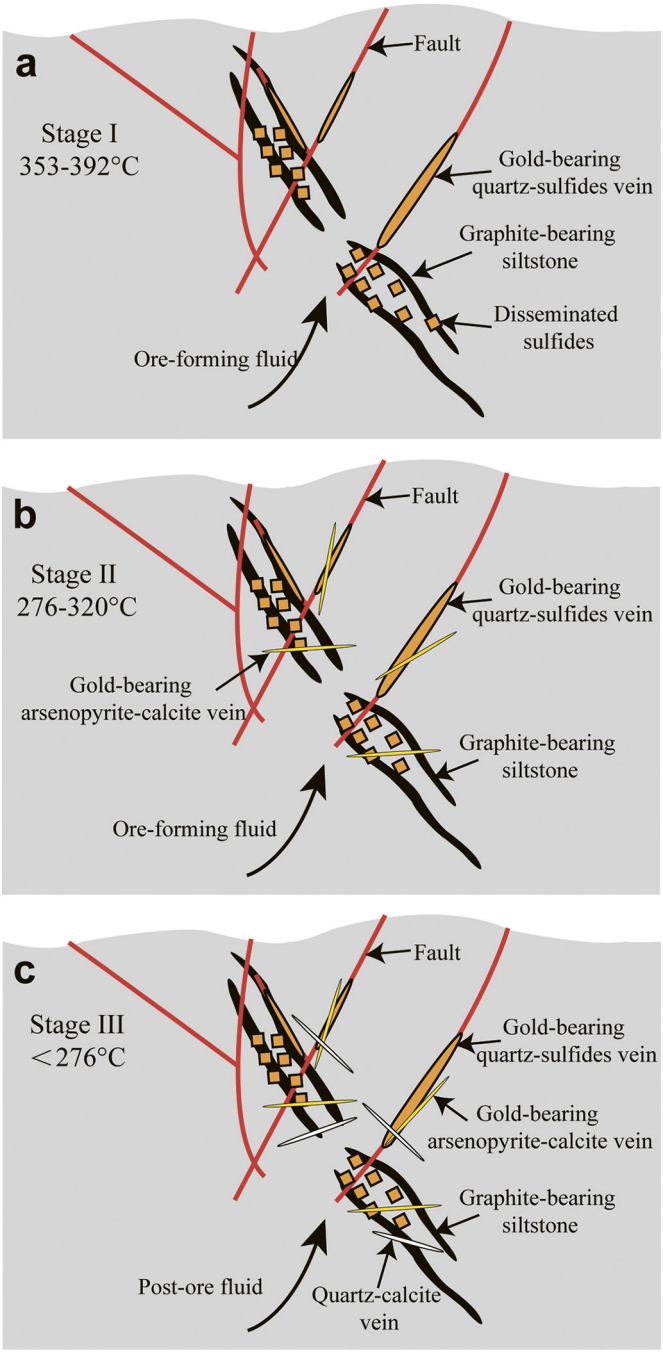

Fig. 12. Genetic model of gold mineralization in the Gezigou mine. (a) Phase separation and the reductive geochemistry barrier provided by graphite in siltstone facilitated gold precipitation in arsenopyrite. (b) Gold-bearing arsenopyrite-calcite veins formed in fractures. (c) Quartz-calcite veins formed with quartz and calcite during post-ore process.

compositions of ore-bearing intrusions suggest that the primary magma at Baogutu was oxidized and became reduced after its emplacement due to contamination with country rocks. Country rocks, including argillaceous silty tuff and argillaceous siliceous rocks, usually contain carbonaceous materials, and their carbon isotope data indicate that these carbonaceous materials participated in the ore-forming process (Shen and Pan, 2015). These phenomena suggest that the graphite and carbonaceous materials-bearing sedimentary rocks in the Gezigou, Mandongshan, and Baobei gold deposits were responsible for the presence of CH_4-rich hydrothermal fluid.

The Late Carboniferous to Early Permian post-collisional magmatism strongly enhanced the hydrothermal fluid activity in the Hatu-Baobei volcanic-sedimentary basin in west Junggar. First, gold-bearing hydrothermal fluids migrated to the Huilvshan-Mandongshan gold district along the Anqi fault zone. Subsequently, the ore-forming fluid migrated to the Mandongshan and Gezigou regions along the secondary faults related to the Anqi fault system. In the Gezigou mine, the ore-forming fluid (353 to 392 °C) intensively interacted with the siltstone (Fig. 12a). The graphite and carbonaceous materials in the siltstone acted as a reductive barrier and facilitated the decrease in fO_2 during this fluid-rock reaction. The ore-forming fluids containing CH_4 may be also attributed to the fluid-rock interaction between the ore-forming fluid and the graphite and carbonaceous materials in the siltstone. Mishra and Pal (2008) showed that the equilibrium between C-H-O fluid and graphite will generate binary H_2O-CH_4 fluid (rather than a CH_4-CO_2-H_2O mixture) over a wide range of O_2 fugacity at temperatures below 500 °C. Phase separation, which occurred in response to the decrease in pressure during the upward migration of the ore-forming fluid, played an important role in the decrease in fS_2 of the ore-forming fluid. The decreases in fS_2 and fO_2 triggered by the fluid-rock reaction and phase separation is the major mechanism causing native gold precipitation in stage I. Stage I is represented by gold-bearing quartz-sulfides veins and disseminated sulfides along the graphite-bearing belt in the siltstone. Gold-bearing arsenopyrite-calcite veins (stage II; 276–320 °C) subsequently formed in fractures, crosscutting the gold-bearing quartz-sulfides veins (Fig. 12b). Finally, the quartz-calcite veins crosscut the previously formed gold-bearing veins (Fig. 12c).

7. Conclusions

In the Gezigou gold deposit, graphite-bearing siltstone is the main wall rock, and arsenopyrite is the dominant sulfide and the only gold-bearing sulfide. The ore-forming fluid was a moderate, low-salinity, H_2O-CH_4 solution. The decrease in a_{H2S} and fO_2 triggered by phase separation and fluid-rock reaction are the dominant mechanisms of gold precipitation. Thermodynamic modeling shows that the Au and As solubilities gradually decrease along with decreases in a_{H2S} and fO_2. This result provides insight into the co-precipitation mechanism of native gold and arsenopyrite. The relative contents of sulfides may be controlled by the redox condition of the ore-forming system, which requires further research.

Acknowledgments

This work was supported by the National Natural Science Foundation of China (Grant no. 41672047) and the China Postdoctoral Science Foundation (Grant no. 2017M620060). We are grateful to Dr. Robert Ayuso, Dr. Alfons van den Kerkhof (University of Goettingen, Germany), and two anonymous reviewers for their critical comments and suggestions. We also give thanks to Dr. Rui Wang and Yuan Mei (CSIRO, Australia) and Dr. Kristopher Fecteau (Arizona State University, USA) for providing some references related to the thermodynamic properties of arsenic hydroxide at elevated temperatures and pressures. Discussions with Dr. Richen Zhong also improved the quality of this paper. Our gratitude is also extended to Greg Hall (senior exploration geologist, Australia) for providing comments and correcting grammatical and syntax errors.

References

An, F., Zhu, Y.F., 2007. Studies on geology and geochemistry of alteration-type ore in the Hatu gold deposit (western Junggar), Xinjiang, NW China. Mineral Deposits 26, 621–633 (in Chinese with English abstract).

An, F., Zhu, Y.F., 2009. SHRIMP U-Pb zircon ages of tuff in Baogutu Formation and their geological significances. Acta Petrol. Sin. 25, 1437–1445 (in Chinese with English abstract).

An, F., Zhu, Y.F., 2018. Geology and geochemistry of the early Permian Axi low-sulfidation epithermal gold deposit in North Tianshan (NW China). Ore Geol. Rev. 100,

12–30.
Ballantyne, J.M., Moore, J.N., 1988. Arsenic geochemistry in geothermal systems. Geochim. Cosmochim. Acta 52, 475–483.
Benning, L.G., Seward, T.M., 1996. Hydrosulphide complexing of Au (I) in hydrothermal solutions from 150–400 °C and 500–1500 bar. Geochim. Cosmochim. Acta 60 (11), 1849–1871.
Bodnar, R.J., 1993. Revised equation and table for determining the freezing point depression of H_2O-NaCl solutions. Geochim. Cosmochim. Acta 57, 683–684.
Cao, M., Qin, K., Li, G., Jin, L., Evans, N.J., Yang, X., 2014. Baogutu: An example of reduced porphyry Cu deposit in western Junggar. Ore Geol. Rev. 56, 159–180.
China National Gold Group Corporation Geology Co., Ltd, 2014. Geological Investigation Report of Gezigou Gold Deposit in Tuoli, Xinjiang. (in Chinese).
Cook, N.J., Ciobanu, C.L., Meria, D., Silcock, D., Wade, B., 2013. Arsenopyrite-pyrite association in an orogenic gold ore: tracing mineralization history from textures and trace elements. Econ. Geol. 108 (6), 1273–1283.
Deditius, A.P., Reich, M., Kesler, S.E., Utsunomiya, S., Chryssoulis, S.L., Walshe, J., Ewing, R.C., 2014. The coupled geochemistry of Au and As in pyrite from hydrothermal ore deposits. Geochim. Cosmochim. Acta 140, 644–670.
Duan, Z., Mao, S., 2006. A thermodynamic model for calculating methane solubility, density and gas phase composition of methane-bearing aqueous fluids from 273 to 523 K and from 1 to 2000 bar. Geochim. Cosmochim. Acta 70, 3369–3386.
Eary, L.E., 1992. The solubility of amorphous As2S3 from 25 to 90 °C. Geochim. Cosmochim. Acta 56, 2267–2280.
Fleet, M.E., Mumin, A.H., 1997. Gold-bearing arsenian pyrite and marcasite and arsenopyrite from Carlin Trend gold deposits and laboratory synthesis. Am. Mineral. 82, 182–193.
Han, B.F., Jian, J.Q., Song, B., Chen, L.H., Zhang, L., 2006. Late Paleozoic vertical growth of continental crust around the Junggar Basin, Xinjiang, China (part I): timing of post-collisional plutonism. Acta Petrol. Sin. 22, 1077–1086 (in Chinese with English abstract).
Heinrich, C.A., 2005. The physical and chemical evolution of low-salinity magmatic fluids at the porphyry to epithermal transition: a thermodynamic study. Mineral. Deposita 39 (8), 864–889.
Heinrich, C.A., Eadington, P.J., 1986. Thermodynamic predictions of the hydrothermal chemistry of arsenic and their significance for the paragenetic sequence of some cassiterite-arsenopyrite-base metal sulfide deposits. Econ. Geol. 81, 511–522.
Hezarkhani, A., Williams-Jones, A.E., Gammons, C.H., 1999. Factors controlling copper solubility and chalcopyrite deposition in the Sungun porphyry copper deposit, Iran. Mineral. Deposita 34 (8), 770–783.
Johnson, J.W., Oelkers, E.H., Helgeson, H.C., 1992. SUPCRT92: a software package for calculating the standard molal thermodynamic properties of minerals, gases, aqueous species, and reactions from 1 to 5000 bar and 0 to 1000°C. Comput. Geosci. 18 (7), 899–947.
Kovalev, K.R., Kalinin, Y.A., Naumov, E.A., Kolesnikova, M.K., Korolyuk, V.N., 2011. Gold-bearing arsenopyrite in eastern Kazakhstan gold-sulfide deposits. Russ. Geol. Geophys. 52 (2), 178–192.
Kretschmar, U., Scott, S.D., 1976. Phase relations involving arsenopyrite in the system Fe-As-S and their application. Can. Mineral. 14, 364–382.
Large, R.R., Danyushevsky, L., Hollit, C., Maslennikov, V., Meffre, S., Gilbert, S., Bull, S., Scott, R., Embsbo, P., Thomas, H., Singh, B., Foster, J., 2009. Gold and trace element zonation in pyrite using a laser imaging technique: implications for the timing of gold in orogenic and Carlin style sediment-hosted deposits. Econ. Geol. 104, 635–668.
Lin, F., Bodnar, R.J., Becker, S.P., 2007. Experimental determination of the Raman CH_4 symmetric stretching ($\nu 1$) band position from 1–650 bar and 0.3–22 °C: Application to fluid inclusion studies. Geochim. Cosmochim. Acta 71, 3746–3756.
Liu, J.J., Dai, H.Z., Zhai, D.G., Wang, J.P., Wang, Y.H., Yang, L.B., Mao, G.J., Liu, X.H., Liao, Y.F., Yu, C., Li, Q.Z., 2015. Geological and geochemical characteristics and formation mechanisms of the Zhaishang Carlin-like type gold deposit, western Qinling Mountains China. Ore Geol. Rev. 64, 273–298.
Mao, S., Duan, Z., Hu, J., Zhang, D., 2010. A model for single-phase PVTx properties of CO_2-CH_4-H_6-N_2-H_2O-NaCl fluid mixtures from 273 to 1273 K and from 1 to 5000 bar. Chem. Geol. 275, 148–160.
Mao, S., Duan, Z., Hu, W., 2009. A vapor–liquid phase equilibrium model for binary CO_2-H_2O and CH_4-H_2O systems above 523 °C for application to fluid inclusions. J. Supercrit. Fluids 50, 13–21.
Mikucki, E.J., 1998. Hydrothermal transport and depositional processes in Archean lode-gold systems: a review. Ore Geol. Rev. 13 (1–5), 307–321.
Mishra, B., Pal, N., 2008. Metamorphism, fluid flux, and fluid evolution relative to gold mineralization in the Hutti-Maski Greenstone Belt, Eastern Dharwar Craton, India. Econ. Geol. 103 (4), 801–827.
Morey, A.A., Tomkins, A.G., Bierlein, F.P., Weinberg, R.F., Davidson, G.J., 2008. Bimodal distribution of gold in pyrite and arsenopyrite: examples from the Archean Boorara and Bardoc shear systems, Yilgarn Craton, Western Australia. Econ. Geol. 103 (3), 599–614.
Oberthür, T., Weiser, T., Amanor, J.A., Chryssoulis, S.L., 1997. Mineralogical siting and distribution of gold in quartz veins and sulfide ores of the Ashanti mine and other deposits in the Ashanti belt of Ghana: genetic implications. Mineral. Deposita 32 (1), 2–15.
Perfetti, E., Pokrovski, G.S., Ballerat-Busserolles, K., Majer, V., Gibert, F., 2008. Densities and heat capacities of aqueous arsenious and arsenic acid solutions to 350 °C and 300 bar, and revised thermodynamic properties of, and iron sulfarsenide minerals. Geochim. Cosmochim. Acta 72 (3), 713–731.
Pitcairn, I.K., Craw, D., Teagle, D.A., 2015. Metabasalts as sources of metals in orogenic gold deposits. Mineral. Deposita 50 (3), 373–390.
Pokrovski, G.S., Akinfiev, N.N., Borisova, A.Y., Zotov, A.V., Kouzmanov, K., 2014. Gold speciation and transport in geological fluids: insights from experiments and physical-chemical modelling. Geol. Soc. Lond., Spec. Publ. 402 (1), 9–70.
Pokrovski, G.S., Gout, R., Zotov, A., Schott, J., Harrichoury, J.C., 1996. Thermodynamic properties and stoichiometry of the arsenic (III) hydroxide complexes at hydrothermal conditions. Geochim. Cosmochim. Acta 60, 737–749.
Pokrovski, G.S., Kara, S., Roux, J., 2002a. Stability and solubility of arsenopyrite, FeAsS, in crustal fluids. Geochim. Cosmochim. Acta 66, 2361–2378.
Pokrovski, G.S., Zakirov, I.V., Roux, J., Testemale, D., Hazemann, J.L., Bychkov, A.Y., Golikova, G.V., 2002b. Experimental study of arsenic speciation in vapor phase to 500 °C: implications for As transport and fractionation in low-density crustal fluids and volcanic gases. Geochim. Cosmochim. Acta 66 (19), 3453–3480.
Potter, R.W., 1977. Pressure corrections for fluid-inclusion homogenization temperatures based on the volumetric properties of the system NaCl-H_2O. J. Res. U.S. Geol. Surv. 5 (5), 603–607.
Qiu, T., Zhu, Y.F., 2015. Geology and geochemistry of listwaenite-related gold mineralization in the Sayi gold deposit, Xinjiang, NW China. Ore Geol. Rev. 70, 61–79.
Reich, M., Deditius, A., Chryssoulis, S., Li, J.W., Ma, C.Q., Parada, M.A., Barra, F., Mittermayr, F., 2013. Pyrite as a record of hydrothermal fluid evolution in a porphyry copper system: a SIMS/EMPA trace element study. Geochim. Cosmochim. Acta 104, 42–62.
Ren, R., Han, B.F., Xu, Z., Zhou, Y.Z., Liu, B., Zhang, L., Chen, J.F., Su, L., Li, J., Li, X.H., Li, Q.L., 2014. When did the subduction first initiate in the southern Paleo-Asian Ocean: new constraints from a Cambrian intra-oceanic arc system in West Junggar, NW China. Earth Planet. Sci. Lett. 388, 222–236.
Roedder, E., 1984. Fluid inclusions. Rev. Mineral. 12, 646.
Rottier, B., Kouzmanov, K., Wälle, M., Bendezú, R., Fontboté, L., 2016. Sulfide replacement processes revealed by textural and LA-ICP-MS trace element analyses: example from the early mineralization stages at Cerro de Pasco, Peru. Econ. Geol. 111 (6), 1347–1367.
Salvi, S., Velásquez, G., Miller, J.M., Béziat, D., Siebenaller, L., Bourassa, Y., 2016. The Pampe gold deposit (Ghana): Constraints on sulfide evolution during gold mineralization. Ore Geol. Rev. 78, 673–686.
Seward, T.M., 1973. Thio complexes of gold and the transport of gold in hydrothermal ore solutions. Geochim. Cosmochim. Acta 37 (3), 379–399.
Seward, T.M., Williams-Jones, A.E., Migdisov, A.A., 2014. The chemistry of metal transport and deposition by ore-forming hydrothermal fluids. Treatise Geochem. Second Ed. 13, 29–57.
Sharp, Z.D., Essene, E.J., Kelly, W.C., 1985. A re-examination of the arsenopyrite geothermometer geothermometer: pressure considerations and applications to natural assemblages. Can. Mineral. 23, 517–534.
Shen, P., Pan, H., 2015. Methane origin and oxygen-fugacity evolution of the Baogutu reduced porphyry Cu deposit in the West Junggar terrain, China. Mineral. Deposita 50 (8), 967–986.
Shen, P., Pan, H.D., Zhu, H.P., 2016. Two fluid sources and genetic implications for the Hatu gold deposit, Xinjiang, China. Ore Geol. Rev. 73, 298–312.
Shen, P., Shen, Y., Pan, H., Wang, J., Zhang, R., Zhang, Y., 2010. Baogutu porphyry Cu-Mo-Au deposit, west Junggar, Northwest China: Petrology, alteration, and mineralization. Econ. Geol. 105 (5), 947–970.
Simmons, S.F., Arehart, G., Simpson, M.P., Mauk, J.L., 2000. Origin of massive calcite veins in the Golden Cross low-sulfidation, epithermal Au-Ag deposit, New Zealand. Econ. Geol. 95 (1), 99–112.
Stefánsson, A., Seward, T.M., 2004. Gold (I) complexing in aqueous sulphide solutions to 500 °C at 500 bar. Geochim. Cosmochim. Acta 68 (20), 4121–4143.
Van Den Kerkhof, A.M., Hein, U.F., 2001. Fluid inclusion petrography. Lithos 55, 27–47.
Velásquez, G., Béziat, D., Salvi, S., Siebenaller, L., Borisova, A.Y., Pokrovski, G.S., Parseval, P.D., 2014. Formation and deformation of pyrite and implications for gold mineralization in the El Callao District, Venezuela. Econ. Geol. 109, 457–486.
Wang, L., Zhu, Y.F., 2015. Multi-stage pyrite and hydrothermal mineral assemblage of the Hatu gold district (west Junggar, Xinjiang, NW China): Implications for metallogenic evolution. Ore Geol. Rev. 69, 243–267.
Wang, R., Cudahy, T., Laukamp, C., Walshe, J.L., Bath, A., Mei, Y., Young, C., Roache, T., Jenkins, A., Roberts, M., Barker, A., Laird, J., 2017. White Mica as a Hyperspectral Tool in Exploration for the Sunrise Dam and Kanowna Belle Gold Deposits, Western Australia. Econ. Geol. 112 (5), 1153–1176.
Wang, R., Zhu, Y.F., 2007. Geology of the Baobei gold deposit in western Juggar and zircon SHRIMP age of its wall-rocks, western Junggar (Xinjiang, NW China). Geol. J. China Univ. 13, 590–602 (in Chinese with English abstract).
Williams-Jones, A.E., Bowell, R.J., Migdisov, A.A., 2009. Gold in solution. Elements 5 (5), 281–287.
Williams-Jones, A.E., Heinrich, C.A., 2005. 100th Anniversary special paper: vapor transport of metals and the formation of magmatic-hydrothermal ore deposits. Econ. Geol. 100 (7), 1287–1312.
Xie, X., 2009. Study on the Ore-forming Fluid of Gold Deposits in West Junggar, Xinjiang. Master Thesis of Jilin University (in Chinese with English Abstract).
Zhang, H.C., Zhu, Y.F., 2016. Geology and geochemistry of the Huilvshan gold deposit, Xinjiang, China: Implications for mechanism of gold precipitation. Ore Geol. Rev. 79, 218–240.
Zhang, H.C., Zhu, Y.F., 2017. Genesis of the Mandongshan gold deposit (Xinjiang, NW China): T-P-fS_2 and phase equilibria constraints from the Au-As-Fe-S system. Ore Geol. Rev. 83, 135–151.
Zhang, H.C., Zhu, Y.F., 2018. Geochronology and geochemistry of the Huilvshan gabbro in west Junggar (NW China): implications for magma process and tectonic regime. Mineral. Petrol. 112 (3), 297–315.
Zhong, J., Chen, Y.J., Chen, J., Qi, J.P., Dai, M.C., 2018. Geology and fluid inclusion geochemistry of the Zijinshan high-sulfidation epithermal Cu-Au deposit, Fujian Province, SE China: implication for deep exploration targeting. J. Geochem. Explor. 184, 49–65.

Zhong, R.C., Brugger, J., Chen, Y.J., Li, W.B., 2015. Contrasting regimes of Cu, Zn and Pb transport in ore-forming hydrothermal fluids. Chem. Geol. 395, 154–164.
Zhong, R.C., Li, W., Chen, Y., Yue, D., Yang, Y., 2013. P-T-X conditions, origin, and evolution of Cu-bearing fluids of the shear zone-hosted Huogeqi Cu-(Pb-Zn-Fe) deposit, northern China. Ore Geol. Rev. 50, 83–97.
Zhu, Y.F., 2017. Study on podiform chromitite and related platinum group mineral(PGM): progress and prospection. Mineral Deposits 36 (4), 775–794 (in Chinese with English Abstract).
Zhu, Y.F., An, F., 2010. Geochemistry of hydrothermal mineralization: taking gold deposit as an example. Earth Sci. Front. 17 (2), 45–52 (in Chinese with English Abstract).
Zhu, Y.F., An, F., Xu, C.Y., Guo, H.T., Xia, F., Xiao, F., Zhang, F.J., Lin, C.X., Qiu, T., Wei, S.N., 2013a. Geology and Au–Cu Deposits in the Hatu and Its Adjacent Region (Xinjiang): Evolution and Prospecting Model. Geological Publishing House, Beijing, pp. 1–162 (in Chinese with English Abstract).
Zhu, Y.F., Chen, B., Xu, X., Qiu, T., An, F., 2013b. A new geological map of the western Junggar, North Xinjiang (NW China): implications for Paleoenvironmental reconstruction. Episodes 36, 205–220.
Zhu, Y.F., Tan, J.J., Qiu, T., 2016. Platinum group mineral (PGM) and Fe-Ni-As-S minerals in the Sartohay chromitite, Xinjiang (NW China): Implications for the mobility of Os, Ir, Sb, and As during hydrothermal processes. Ore Geol. Rev. 72, 299–312.
Zhu, Y.F., Xu, X., Luo, Z.H., Shen, P., Ma, H.D., Chen, X.H., An, F., Wei, S.N., 2014. Geological Evolution and Ore Formation in the Core Part of Central Asian Metallogenic Region. Geological Publishing House, Beijing, pp. 1–202 (in Chinese with English Abstract).